2017

Depolarization In Nanowires, Tribo–chemistry, And Negative Electrocaloric Effect

Yubo Qi
University of Pennsylvania, yuboqi@sas.upenn.edu

Depolarization In Nanowires, Tribo–chemistry, And Negative Electrocaloric Effect

Abstract
This thesis contains investigations about several technologically--important scientific problems: depolarization process in BaTiO$_3$ nanowires, tribopolymer formation on metal surfaces, and negative electrocaloric effect in prototype ferroelectrics. Spontaneous electric polarization makes perovskite--based oxides of great interest for application to nonvolatile memory devices. However, the polarization of ferroelectric materials may not be infinitely stable. For successful technology application, the depolarization processes of nanoscale ferroelectric oxides must be better understood. Here, we report a combined experimental and theoretical investigation of the depolarization process of single--crystalline BaTiO$_3$ nanowires. By building an Modified Schottky emission model, we explain the both temperature and nanowire thickness dependent polarization decay rates successfully. Besides, Micro--electro--mechanical system and nano--electro--mechanical system (MEMS and NEMS) transistors are considered promising for size--reducing and power--maximizing electronic devices. However, the tribopolymer which forms due to the mechanical load to the surface contacts affects the conductivity between the contacts dramatically. This is one of the challenging problems that prevent widespread practical use of these otherwise promising devices. Here, we use density functional theory (DFT) to investigate the mechanisms of tribopolymer formation,

including normal mechanical loading, the catalytic effect, as well as the electrochemical effect of the metal contacts. Our study illustrates the underlying mechanisms of tribopolymer formation clearly, which has great significance in designing tribopolymerization--suppressing strategies. The last work is about electrocaloric effect. The electrocaloric effect (ECE) refers to the phenomenon in which the temperature of a material changes reversibly under the application and removal of electric field. Here, we point out that negative unusual electrocaloric effect (uECE) with a fast cooling rate ($\approx$10^{11} K/s) can be achieved by driving solid crystals to a high--temperature phase with a properly designed electric field pulse. We acquire and analyze these results by clarifying the mechanism of ECE. Our work offers a more general framework to understand the ECE and highlights the opportunities of electric--field engineering for controlled design of fast and efficient cooling technology.

Degree Type
Dissertation

Degree Name
Doctor of Philosophy (PhD)

Graduate Group
Chemistry

First Advisor
Andrew M. Rappe

DEPOLARIZATION IN NANOWIRES, TRIBO–CHEMISTRY, AND NEGATIVE ELECTROCALORIC EFFECT

Yubo Qi

A DISSERTATION

in

Chemistry

Presented to the Faculties of the University of Pennsylvania in Partial Fulfillment of the Requirements for the Degree of Doctor of Philosophy

2017

Supervisor of Dissertation	Graduate Group Chairperson
Andrew M. Rappe	Joseph E. Subotnik
Professor of Chemistry and Materials Science and Engineering	Professor of Chemistry

Dissertation Committee

Joseph E. Subotnik	Professor of Chemistry
Zahra Fakhraai	Assitant Professor of Chemistry
Jonathan E. Spanier	Professor of Materials Science, Drexel University

To my beloved wife Joy,

for giving me a wonderful life

Acknowledgements

Six years ago, I arrived at Philadelphia, with excitement for future and anxiety for uncertainty. Time flies and six years passed, I am graduating, and recalling with nostalgia. During these years, I learned a lot, gained a lot and have many people who I want to acknowledge.

First, I want to thank my research advisor, Professor Andrew Rappe. He is always willing to share and teach with great patience and tolerance. I still remember that the manuscript of my first publication was proofread and revised by Professor Rappe for as many as nine times. During this process, I really improved a lot and learned a lot. Day by day, I accumulated experience, achievements, confidence and true pleasure from discovering. What I learn from Professor Rappe are not only knowledge about physics, techniques for computing or skills for communication, but also the spirit of perseverance, the bravery of thinking critically, and the enthusiasm for exploring. I am so grateful that I have Professor Rappe as my research advisor, who built my academic characteristics, which I can benefit from always.

I would like to thank Dr. Shi Liu and Dr. Hiroyuki Takenaka for teaching me so much about the bond valence model. We also had many joyful discussions and decent collaborated works.

I thank Dr. Mark Martirez and Ms. Jing Yang for our wonderful collaborations.

I want to thank my committee members Professor Joseph Subotnik, Professor Jonathan

Spanier and Professor Zahra Fakhraai. Their helpful suggestions and feedback provided me the directions for improvement.

I also want to thank Professor Aaron Lindenberg, Professor Lane Martin, Professor Robert Carpick, Professor David Srolovitz, Professor Maarten de Boer, Professor Gianluca Piazza for productive discussions and their meaningful instructions.

Finally, I want to express my gratitude to my wife and parents. I have their support and love always.

ABSTRACT

DEPOLARIZATION IN NANOWIRES, TRIBO–CHEMISTRY, AND NEGATIVE ELECTROCALORIC EFFECT

Yubo Qi

Andrew M. Rappe

This thesis contains investigations about several technologically–important scientific problems: depolarization process in $BaTiO_3$ nanowires, tribopolymer formation on metal surfaces, and negative electrocaloric effect in prototype ferroelectrics. Spontaneous electric polarization makes perovskite–based oxides of great interest for application to nonvolatile memory devices. However, the polarization of ferroelectric materials may not be infinitely stable. For successful technology application, the depolarization processes of nanoscale ferroelectric oxides must be better understood. Here, we report a combined experimental and theoretical investigation of the depolarization process of single–crystalline $BaTiO_3$ nanowires. By building an Modified Schottky emission model, we explain the both temperature and nanowire thickness dependent polarization decay rates successfully. Besides, Micro–electro–mechanical system and nano–electro–mechanical system (MEMS and NEMS) transistors are considered promising for size–reducing and power–maximizing electronic devices. However, the tribopolymer which forms due to the mechanical load to the surface contacts affects the conductivity between the contacts dramatically. This is one of the challenging problems that prevent widespread practical use of these otherwise promising devices. Here, we use density functional theory (DFT) to investigate the mechanisms of tribopolymer formation, including normal mechanical loading, the catalytic effect, as well as the electrochemical effect of the metal contacts. Our study illustrates the underlying mechanisms of tribopolymer formation clearly, which has great significance in designing tribopolymerization–suppressing strategies. The last work is about electrocaloric

effect. The electrocaloric effect (ECE) refers to the phenomenon in which the temperature of a material changes reversibly under the application and removal of electric field. Here, we point out that negative unusual electrocaloric effect (uECE) with a fast cooling rate ($\approx 10^{11}$ K/s) can be achieved by driving solid crystals to a high–temperature phase with a properly designed electric field pulse. We acquire and analyze these results by clarifying the mechanism of ECE. Our work offers a more general framework to understand the ECE and highlights the opportunities of electric–field engineering for controlled design of fast and efficient cooling technology.

Contents

List of Tables

List of Figures

Chapter 1

Depolarization in $BaTiO_3$ nanowires

DOI: https://doi.org/10.1103/PhysRevB.91.245431

1.1 Introduction

Spontaneous electric polarization makes perovskite-based oxides of great interest for application to nonvolatile memory devices [1, 2]. However, the polarization of ferroelectric materials may not be infinitely stable, and retention time is one of the key factors determining the performance of memory devices in nonvolatile technology. The proposed reasons for the polarization instability have included the depolarization field and the leakage cur-

rent [3], whose effects become more significant as the oxide film gets thinner. Therefore, for successful technology application, the depolarization processes of nanoscale ferroelectric oxides must be better understood. Here, we report a combined experimental and theoretical investigation of the depolarization process of single–crystalline $BaTiO_3$ nanowires. We attribute the decay of polarization to the leakage of surface screening charge and propose an analytical model to explain the experimental decay rates.

1.1.1 Experimental background

The effects of the depolarization field on the stability of ferroelectricity in ultrathin materials was explored in $BaTiO_3$ nanowires by measuring the ferroelectric transition temperature as a function of the nanowire diameter in the range of 3–48 nm [4, 5, 6, 7]. Positive ferroelectric domains were written perpendicular to the nanowire axis using a negative-bias voltage (-10 V) applied by a conductive scanning probe microscope cantilever tip (under ultrahigh vacuum conditions with a base pressure of 10^{-10} torr). The time evolution of the polarized domain was then monitored via time-resolved measurements of the local electric field, using non-contact electrostatic force microscopy (EFM). The writing and reading processes were done at various temperatures, starting from $\approx$ 393 K for thin nanowires (3–11 nm) and ≈ 418 K for the thicker ones (12–37 nm). The two sets of nanowires were progressively cooled down and retested to $\approx$ 308 K and $\approx$ 383 K were reached respectively. The Curie temperature T_C was defined as the highest temperature below which the polarization signal persists for a period longer than 200 hours. Experiments showed that T_C is inversely proportional to the diameter of the $BaTiO_3$ nanowire, in accord with standard models of depolarization field [8]. At several temperatures above T_C, the surface potential signals were measured during the process of polarization decay. The magnitude of surface

potential was fitted with the expression:

$$S(t) = S(0)e^{-k_d t} \tag{1.1}$$

where $S(t)$ is the potential at time t, which is proportional to the surface screening charge, and k_d is the decay rate, with the unit s^{-1} [9]. Here, we should note that experimentally it is found that the signals decay with time approximately (but not perfectly) exponentially. Despite the slight deviations, the decay rate k_d obtained from the data fitting is still an important physical parameter in describing the polarization decay speed. From the time evolution of the signal [4], we see that the bright circular signal faded without expansion, which means that the depolarization is a process of leakage or tunneling, rather than diffusion, of the surface screening charge. The observed decay rates k_d, which vary with nanowire thickness and temperature, are shown in Fig. 1.1 (please refer to the red circles).

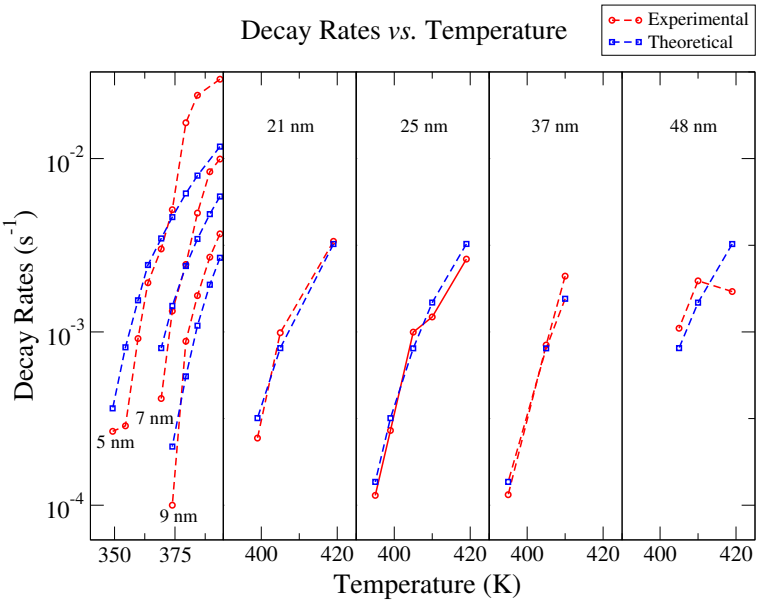

Figure 1.1: Depolarization rates given by experimental measurement and our model.

The experimental data show three general trends: (1) The depolarization process is slow (several hours); (2) For any thickness, the decay rate k_d increases with temperature;

(3) For thin nanowires (5–9 nm), the decay rate k_d changes with thickness dramatically. However, for thicker wires, k_d stays nearly constant at different thicknesses (21, 25, 37 and 48 nm). Our study aims at illustrating the physical essence of these trends.

1.1.2 Polarization stabilization

In recent years, many studies have investigated the dependence of polarization stabilization and leakage current on chemical environment, temperature, electrode material, and thickness [4, 8, 10, 11, 12, 13, 14, 15, 16, 17, 18, 19, 20, 21, 22, 23, 24, 25, 26, 27, 28]. From these studies, several basic principles could be drawn:

(1) Surface polarization charge should be compensated by screening charge, in order to passivate the depolarization field and stabilize the ferroelectric distortion, or else the polarization would become unstable. The screening charge could be stored in surface electrodes or adsorbates [8, 10, 11, 12, 13, 14, 15, 16, 17, 18];

(2) The polarization state of the material may lead to preferential adsorption of certain molecules on the surface [19, 20, 21, 22, 23, 24, 25];

(3) The response of polarization with electric field or temperature is fast, but the time scale for dissipation of the surface screening charge is slow (hours or days) [26, 27, 28].

Based on the evidence above and the observations in our experiments, we propose that the physical process of depolarization in the $BaTiO_3$ nanowire experiment is as follows: after the polarization is written, surface adsorbates on the nanowire act as an electrode that stores screening charge and stabilizes the polarization [4]. For the case without external applied voltage and above T_C, the polarized state is not stable. But due to the stabilization of screening charge in the surface adsorbates, polarization in the nanowire still persists for

some time. Screening charge leaks from the top electrode (surface adsorbate) to the other side of the $BaTiO_3$ nanowire (gold substrate). At the same time, polarization reduces along with the screening charge. This process is slow and takes hours.

1.2 DFT calculations

In order to construct a theory of the depolarization process, density functional theory calculations (DFT) are carried out to assess the role of surface molecular and atomic adsorbates. We investigate the OH molecule on BaO-terminated $BaTiO_3$ slabs, as OH is the predominant species found on oxide surfaces, as demonstrated by both infrared spectra and $ab\ initio$ calculations [4, 29, 30].

Density functional theory (DFT) calculations with periodic boundary conditions were carried out using the QUANTUM–ESPRESSO plane–wave DFT code [31]. The exchange–correlation functional was approximated with the Perdew–Burke–Ernzerhof form of the generalized gradient scheme. Plane–wave cut–off energy of 50 Ry was used in all calculations. The pseudopotentials were generated using the OPIUM code following the norm–conserving designed non-local recipe [32, 33]. 1×1 five–unit–cell–thick $BaTiO_3$ slabs, separated by more than 20 Å of vacuum normal to the surface, were used to simulate the thin films. Additional dipole correction was added in the middle of the vacuum to further correct the spurious electric field interaction between periodic images. A k–point mesh of $6\times6\times1$ was used following the Monkhorst-pack sampling scheme [34]. Atomic forces were converged until a maximum threshold of 0.05 eV/Å per atom is reached.

As shown in Fig. 1.2, from the relaxed structure, we see that the presence of the OH adsorbates enhances ferroelectricity at the positively polarized surface and maintains a characteristic ferroelectric displacement pattern throughout the film, which is consistent with the results in Ref. [4].

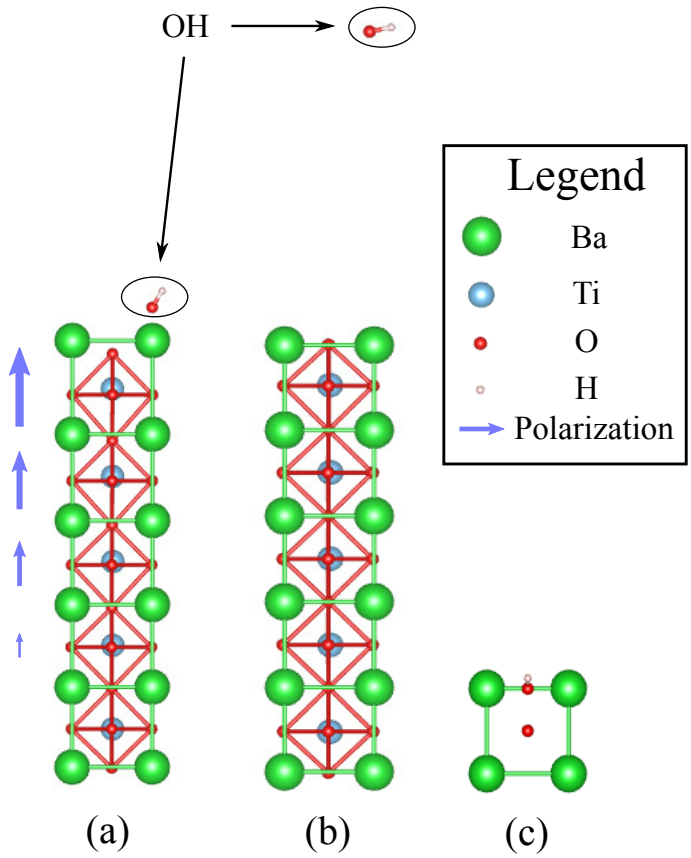

Figure 1.2: Relaxed structures for the $BaTiO_3$/OH systems acquired from DFT calculation. (a) Polar system; (b) Non–polar structure; (c) Top view.

	Polar	Non-polar
H $1s$ orbital	0.6121	0.5601
O $2s$ orbital	1.7315	1.8138
O $2p$ orbital	5.0719	4.5980
Net Charge	-0.4155	0.0289

Table 1.1: Löwdin population in the orbitals of OH.

The density of states projected onto atomic orbitals (PDOS) was calculated to characterize the charge distribution on each atom. Results are shown in Table 1.1, from which we see that if the $BaTiO_3$ nanowire is positively polarized, the hydroxyl oxygen $2p$ orbital possesses more electrons and OH is overall negatively charged. This is a robust evidence demonstrating that surface adsorbates stabilize the polarization by holding screening charges, which has an effect similar to an electrode. The leakage of charge mainly from the $2p$ orbital of oxygen then results in the decay of polarization.

1.3 Formalism of leakage current

There have been previous reports calculating the magnitude of leakage through ferroelectric films with tunneling models, Schottky emission, and the modified Schottky equation [35, 36, 37]. However, all these models come across difficulties in explaining all three depolarization rate trends mentioned above. A tunneling model alone cannot explain that for thick nanowires, decay rates are nearly thickness independent and for any thickness, the decay rates are strongly temperature dependent. On the other hand, a Schottky emission model cannot account for the thin nanowire thickness dependent rates. Here, we build a comprehensive model from the "effective velocity" point of view, which both accounts for the experimental results and illustrates their physical mechanisms.

The general expression for the time (t) dependent leakage current J can be written as

$$-\frac{\partial Q\left(t\right)}{\partial t}=J\left(t\right)=\int Q\left(t\right)n\left(\boldsymbol{k}\right)v_{\text{eff}}\left(\boldsymbol{k}\right)d^{3}\boldsymbol{k} \tag{1.2}$$

where $n\left(\boldsymbol{k}\right)$ is the probability that an electron possesses a wave vector between $\boldsymbol{k}$ and $\boldsymbol{k}+d\boldsymbol{k}$. $v_{\text{eff}}\left(\boldsymbol{k}\right)$ is the effective velocity along the z direction, which is normal to the surface of the $BaTiO_3$ nanowire, for the electrons with wave vector $\boldsymbol{k}$. Q is the amount of extra charge

(compared with neutral OH) stored in the adsorbate. In the following subsections, we define the parameterization of equation (1.2).

1.3.1 Wave vector distribution

Unlike in traditional metal electrodes, electrons occupying orbitals localized on the OH adsorbates cannot be treated as a free electron gas, and the wave vector distribution does not follow Fermi-Dirac statistics. Instead, the wave vector spectrum can be estimated from Bessel-Fourier transformation of the $2p$ orbital of oxygen, since screening charge is mainly associated with this atomic orbital. Here, the radial part of the $2p$ orbital of the oxygen is represented by a double–zeta function [38].

$$\begin{aligned}
\phi_{2p}(\boldsymbol{r}) &= R(r)\, Y_{10}(\theta_r, \phi_r) \\
&= \left(c_1 \sqrt{\frac{(2z_1)^5}{4!}} r e^{-z_1 r} + c_2 \sqrt{\frac{(2z_2)^5}{4!}} r e^{-z_2 r} \right) Y_{10}(\theta_r, \phi_r) \\
&= \left(c_1' r e^{-z_1 r} + c_2' r e^{-z_2 r} \right) Y_{10}(\theta_r, \phi_r)
\end{aligned} \tag{1.3}$$

$$\begin{aligned}
\phi_{2p}(\boldsymbol{k}) &= \frac{1}{(2\pi)^{3/2}} \int e^{-i\boldsymbol{k}\cdot\boldsymbol{r}} \phi_{2p}(\boldsymbol{r})\, d^3\boldsymbol{r} \\
&= -\sqrt{\frac{8}{\pi}} 4i Y_{10}(\theta_k, \phi_k) \left[\frac{c_1' z_1 k}{(z_1^2 + k^2)^3} + \frac{c_2' z_2 k}{(z_2^2 + k^2)^3} \right]
\end{aligned} \tag{1.4}$$

$$n(\boldsymbol{k}) = |\phi_{2p}(\boldsymbol{k})|^2 = \frac{128}{\pi} |Y_{10}(\theta_k, \phi_k)|^2 \left[\frac{c_1' z_1 k}{(z_1^2 + k^2)^3} + \frac{c_2' z_2 k}{(z_2^2 + k^2)^3} \right]^2 \tag{1.5}$$

where Y_{10} is the spherical harmonic for $l = 1$ and $m = 0$. $c_{1,2}$ and $z_{1,2}$ are the parameters in the double–zeta function, acquired from previous reference [38]. c_1' and c_2' are reduced coefficients taking the normalization factors $\sqrt{\frac{(2z_1)^5}{4!}}$ and $\sqrt{\frac{(2z_2)^5}{4!}}$ into consideration. $\theta_{r,k}$ and $\phi_{r,k}$ are the angles between the directions of $\boldsymbol{r}$, $\boldsymbol{k}$ and the axes in spherical coordinates. $\phi_{2p}(\boldsymbol{r})$ and $\phi_{2p}(\boldsymbol{k})$ are expressions for the oxygen $2p$ wavefunction in coordinate and wave

vector representations. In this way, we obtain an analytical expression for $n(\boldsymbol{k})$. Here, we should note that in part II, we used pseudo wavefunctions in the DFT calculations; compared with all–electron wavefunctions, pseudo wavefunctions have lower high–k components on purpose to limit the number of plane waves used [39]. This does not affect the accuracy of charge leakage rate calculation. This is because the DFT calculation is used only to illustrate the role of screening charge and the mechanism of the depolarization process. The wave-vector distribution in this model is derived from the double-zeta function as described above. Additionally, in the later discussion, we will also include the fact that high–speed electrons lose their initial momentum quickly and drift under the effect of the electric field. Therefore, an underestimation of the high–k components has little effect on the charge dissipation speed.

1.3.2 Effective velocity

Here, we present an effective velocity model of the charge dissipation. The band diagram of the OH/$BaTiO_3$/Au substrate system is shown in Fig. 1.3 (a).

We only consider the effective velocities of the electrons with the wave vector pointing toward the nanowire $\boldsymbol{k} \cdot \hat{\boldsymbol{z}} > 0$. Otherwise, the electron does not contribute to the leakage current J and its effective velocity $v_{\text{eff}} = 0$. For the electron moving toward the nanowire, the expression for effective velocity varies depending on whether the energy of the electron is higher than that of $BaTiO_3$ conduction band edge. The potential energy of an electron affiliated with the hydroxyl molecule oxygen $2p$ orbital is set as V_0. The total energy for this electron can be written as the sum of its kinetic energy $T(\boldsymbol{k})$ and V_0:

$$E(\boldsymbol{k}) = T(\boldsymbol{k}) + V_0 = \frac{\hbar^2 |\boldsymbol{k}|^2}{2m_0} + V_0. \tag{1.6}$$

As shown in Fig. 1.3 (a), the conduction band for the $BaTiO_3$ nanowire is not flat, and

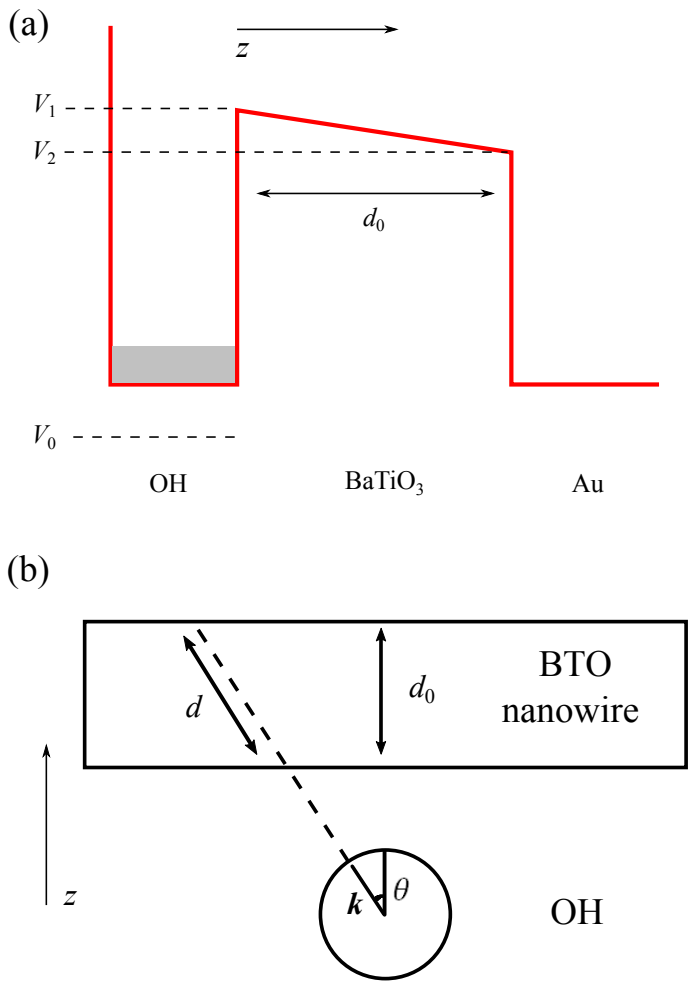

Figure 1.3: (a) Band diagram of the Au electrode/oxide insulator/adsorbate electrode system; (b) Relationship of barrier thickness and direction of wave vector.

the slope equals the electronic charge e times the electric field E_{fe} inside the ferroelectric nanowire. Therefore,

$$V_2 = V_1 - eE_{\mathrm{fe}}d_0, \tag{1.7}$$

For the case $E(\boldsymbol{k}) < V_2$, the mechanism that governs the electron movement is quantum tunneling. The electron tunnels from the surface adsorbate hydroxyl to the gold electrode at the other side, through the $BaTiO_3$ nanowire as an energy barrier. Around T_C, the dielectric constant of $BaTiO_3$ is large and E_{fe} is small. Therefore, the conduction band is nearly flat and we use the approximation that the energy barrier is a cuboid with the height V_2. The transmission coefficient $P(\boldsymbol{k})$, which is also the probability of one electron with wave vector $\boldsymbol{k}$ penetrating the barrier, could be expressed [40]:

$$P(\boldsymbol{k}) = \frac{4}{4 + \dfrac{\left[m_0 E + m^*(V_2 - E)\right]^2}{m_0 m^* E(V_2 - E)} \sinh^2 \left[\dfrac{2m^* d^2 (V_2 - E)}{\hbar^2}\right]^{1/2}} \tag{1.8}$$

where d is the length of the barrier. m^* is the effective mass of electrons in $BaTiO_3$. Assuming that the angle between the incident direction of the electron and the normal direction of the $BaTiO_3$ nanowire is θ, as shown in Fig. 1.3 (b), d could be expressed as

$$d = \frac{d_0}{\cos\theta}. \tag{1.9}$$

In this tunneling process, an electron with an initial velocity $v = \frac{\hbar \boldsymbol{k}}{m_0}$ has a probability $P(\boldsymbol{k})$ of passing the energy barrier with the thickness d. Thus, the effective velocity could be expressed as

$$v_{\mathrm{eff}}(\boldsymbol{k}) = vP(\boldsymbol{k}) = \frac{\hbar \boldsymbol{k} \cdot \hat{\boldsymbol{z}}}{m_0} P(\boldsymbol{k}) = \frac{\hbar k \cos\theta}{m_0} P(\boldsymbol{k}). \tag{1.10}$$

When the hydroxyl electron energy is higher than that of the $BaTiO_3$ conduction band edge $E(\boldsymbol{k}) > V_1$, the electron is not classically forbidden to enter the $BaTiO_3$ nanowire.

However, very high velocity electrons could have very short mean free paths. Moreover, in the $BaTiO_3$ crystal, which is an insulator and possesses a small mean free path [41], the electron loses its initial momentum quickly and drifts under the effect of electric field E_{fe} inside the ferroelectric nanowire:

$$v_{\mathrm{eff}} = \mu E_{\mathrm{fe}}, \tag{1.11}$$

where μ is the electronic mobility, which depends on temperature, intermediate energy levels and lattice vibrations. Lattice vibrations have a significant influence on the drift mobility due to electron-phonon interactions [42, 43, 44, 45], in which an electron may lose or gain energy in a collision. This effect will be discussed in the following subsection.

For the final case, $V_2 < E(\boldsymbol{k}) < V_1$, the electron first tunnels through an energy barrier and then drifts in the conduction band. The effective velocity is given by

$$v_{\mathrm{eff}} = \mu E_{\mathrm{fe}} P(\boldsymbol{k}). \tag{1.12}$$

For this case, the energy barrier goes to zero within the nanowire. At this condition, the Wentzel–Kramers–Brillouin (WKB) [46] approximation fails. Since $E(\boldsymbol{k})$ is close to V_1, we approximate $P(\boldsymbol{k})$ to 1.

Even though the approximations in the first and last cases overestimate the tunneling current, later we will point out that despite this, the tunneling current is still a negligible contribution to the overall current.

1.3.3 Electric Properties of $BaTiO_3$ Nanowire

The relationship of surface charge density Q, electric displacement D_{fe} and electric field E_{fe} though the insulator is given by dielectric constant $\epsilon\left(T\right)$ [11]:

$$Q\left(t\right) = D_{\mathrm{fe}} = \epsilon\left(T\right)\epsilon_0 E_{\mathrm{fe}}. \tag{1.13}$$

According to the Lyddane-Sachs-Teller [47] relation, the temperature dependent static dielectric constant is expressed as:

$$\frac{\epsilon\left(T\right)}{\epsilon_\infty} = \frac{\prod_i \omega_{L_i}^2\left(T\right)}{\prod_i \omega_{T_i}^2\left(T\right)} \tag{1.14}$$

where ω is the frequency of lattice vibration and T_i and L_i represent transverse and longitudinal modes. Approaching T_C, a transverse optical mode ω_{TO} becomes "soft", indicating the occurrence of phase transition [48, 49, 50]:

$$\omega_{\mathrm{TO}}^2 \approx A\left(T - T_C\right) \tag{1.15}$$

$$\epsilon\left(T\right)^{-1} \propto \omega_{\mathrm{TO}}^2 = A'\left(T - T_C\right) \tag{1.16}$$

where A and A' are constants, and for $BaTiO_3$ bulk [51, 52], $T_C \approx 393$ K. However, for a thin film or nanowire, if polarization exists, a depolarization field is induced due to the incomplete charge compensation of polarization charge [53, 54, 13]. The depolarization field, which is anti–parallel to polarization, becomes significant as the thickness decreases. It also applies an electric force on the ions, and as a consequence, the soft vibrational mode is hardened. With the depolarization field effect included, the temperature dependent soft

mode frequency for thin films should be rewritten as

$$\omega_{\mathrm{TO}}^2 \approx A\left(T - T_C'\right) \tag{1.17}$$

$$\epsilon\left(T\right)^{-1} = A'\left(T - T_C'\right) \tag{1.18}$$

and

$$T_C' < T_C. \tag{1.19}$$

The depolarization field effect hardens the soft mode, increases the vibrational frequency, suppresses the ferroelectricity and lowers the T_C. The values of T_C' for different thicknesses could be inferred from T_C, which were previously experimentally measured [4].

Previous studies illustrated that the electronic mobility in $BaTiO_3$ varies over a large range (10^{-3}–10^{-1} cm^2/V–s) [55, 56, 45]. The variation of mobility could be attributed to the different trap levels, types and concentrations from the fabrication process. Despite the uncertainty, there is a general rule that electron mobility is determined by the optical phonons [42, 43, 44, 45].

Many studies in recent years pointed out that scattering by the soft transverse optical mode is the primary factor affecting electron drift [45, 57, 58]. In this case [58]:

$$\mu = \frac{f\left(T\right)}{\epsilon\left(T\right)} \propto f\left(T\right)\omega_{\mathrm{TO}}^2 \tag{1.20}$$

and $f\left(T\right)$ depends weakly on T for $BaTiO_3$ [58, 57]. For $T > T_C'$

$$\mu \approx B\omega_{\mathrm{TO}}^2 = B'\left(T - T_C'\right) \tag{1.21}$$

where B and B' are constants. An explicit explanation about the soft mode dependent

mobility was proposed in Ref. [45]. In brief, according to thermodynamics, the mean squared polarization fluctuation δP is related to the dielectric constant as [59].

$$\langle \delta P^2 \rangle = k_B T \epsilon / V \propto 1/\omega_{\mathrm{TO}}^2 \tag{1.22}$$

where k_B is Boltzmann constant and V is the volume. For the case $T > T_C'$, a high soft mode frequency means a small dielectric constant, large mean–square TO phonon amplitude and polarization fluctuation. Besides, in a small region with an approximately uniform polarization fluctuations, shifts in the conduction band edge $\Delta \mathcal{E}_c$ is [60]

$$\Delta \mathcal{E}_c = \mathrm{const} + \beta \delta P^2 \tag{1.23}$$

where β is the polarization–potential parameter, which has a typical value $\beta \approx 2$ eV m^4/C^2. In the nanowire, the low soft mode frequency leads to inhomogeneity in $\Delta \mathcal{E}_c$, which then results to locally different effective masses and electronic energies. Therefore, an electron traveling through the wire scatters more. This is similar to an electron traveling on a curved path and harder to accelerate. A lower soft mode frequency means more scattering, a shorter relaxation time, τ_e, and a smaller electron mobility, since electron mobility is given by [61]

$$\mu = \frac{e\tau_e}{m^*} \tag{1.24}$$

Thus, in this simulation, we use the empirical expression of electron mobility as shown in equation (1.21).

1.4 Results and discussions

With the expressions of effective velocity deduced in different wave vector range,

$$v_{\text{eff}}(\boldsymbol{k}) = \begin{cases} \frac{\hbar \boldsymbol{k}}{m} \cdot P(\boldsymbol{k}) & \text{if } E(\boldsymbol{k}) < V_2, \boldsymbol{k} \cdot \hat{\boldsymbol{z}} > 0 \\ \mu E_{\text{fe}} P(\boldsymbol{k}) & \text{if } V_2 < E(\boldsymbol{k}) < V_1, \boldsymbol{k} \cdot \hat{\boldsymbol{z}} > 0 \\ \mu E_{\text{fe}} & \text{if } E(\boldsymbol{k}) > V_1, \boldsymbol{k} \cdot \hat{\boldsymbol{z}} > 0 \\ 0 & \text{if } \boldsymbol{k} \cdot \hat{\boldsymbol{z}} < 0, \end{cases} \tag{1.25}$$

we could calculate the time evolution of surface charge with equation (1.2).

The expression of current density was shown in equation (1.2). In the calculation of charge density evolution with time, the initial charge density used in the simulation is $Q(0) = 0.26$ C/m^2 [32], which is the spontaneous polarization for the tetragonal phase of $BaTiO_3$. The time window is selected as 10^4 s, which is long enough to demonstrate the general trend of time evolution of surface charge in adsorbate OH. Other parameters involved in the presented tunneling and modified Schottky model are listed in Table 1.2. Most of the parameters are from previous references. The difference of the potential energy of electrons in the adsorbate oxygen $2p$ orbital (V_0) and in the conduction band formed by titanium $3d$ orbitals (V_1)

is estimated from the band gap of $BaTiO_3$ (3.20 eV) [62]. This is a good approximation because the adsorbate oxygen $2p$ orbital is approximately at the same level with the valence band formed by oxygen $2p$ orbitals of the nanowire.

$$V_1 - \overline{E(\boldsymbol{k})} \approx 3.20 \text{ eV} \tag{1.26}$$

where $\overline{E(\boldsymbol{k})}$ is the average energy of electrons in the adsorbate oxygen $2p$ orbital, and

$$\overline{E(\boldsymbol{k})} = \overline{T(\boldsymbol{k})} + V_0 \tag{1.27}$$

$$\overline{T(\boldsymbol{k})} = \int_0^\infty n(\boldsymbol{k}) \frac{\hbar^2 \boldsymbol{k}^2}{2m_0} d^3\boldsymbol{k} = 68.28 \text{ eV} \tag{1.28}$$

$$V_1 - V_0 = V_1 - \overline{E(\boldsymbol{k})} + \overline{T(\boldsymbol{k})} = 71.48 \text{ eV}. \tag{1.29}$$

In the modeling, the surface charge density Q decays with time t, but not exactly exponentially. We fit each Q *vs.* t curve with an exponential function by the least squares fitting method. In this way, we obtain decay constants from this model that can be compared with experimental ones. B' of equation (1.21) is the only parameter calculated by fitting the data in experiments to the decay rates calculated by this analytical model, rather than from any references or $ab\ initio$ calculation.

The decay rates calculated from this model and experimental data are shown in Fig. 1.1. Experimental data are marked with red circles and theoretically calculated ones are blue squares. Symbols for decay rates of a given thickness are connected with dashed lines, to demonstrate their temperature dependence. From the comparison, it could been seen that this model not only simulates the experimental results to a good extent, but also sheds light on the general rules of ferroelectric leakage current.

For nanowires with any thicknesses, calculations based on equations (1.2) and (1.25) demonstrate that tunneling current provides a negligible part of the total leakage current. Even for the thinnest nanowires (5 nm) with a surface charge density $Q(0) = 0.26$ C/m^2, the tunneling current is around 10^{-6} A/m^2 or less, generally no more than 1 percent of the total leakage current. Emission of electrons with energies higher than the barrier con-

Parameter	Description	Value
T_C' (5 nm)	T_C for 5 nm nanowire[a]	340.3 K
T_C' (7 nm)	T_C for 7 nm nanowire[a]	355.2 K
T_C' (9 nm)	T_C for 9 nm nanowire[a]	367.9 K
T_C	T_C for thick nanowires[a]	391 K
c_1	Parameter in equation (1.3)[b]	0.72540
c_2	Parameter in equation (1.3)[b]	0.35173
z_1	Parameter in equation (1.3)[b]	1.62807 bohr^{-1}
z_2	Parameter in equation (1.3)[b]	3.57388 bohr^{-1}
m^*	Effective electronic mass	6.5 m_0
$V_1 - V_0$	Energy barrier[d]	71.48 eV
A'	Defined in equation (1.18) [e]	7.84×10^{-6} K^{-1}
B'	Defined in equation (1.21) [f]	5.025×10^{-6}

Table 1.2: Parameters involved in the modified Schottky model.

[a] Reference [4]
[b] Reference [38]
[c] Reference [55]
[d] From the band gap estimation
[e] Estimated from reference [52]
[f] The unit is cm^2/VsK

tributes nearly all the current. The fact that tunneling, whose rate is thickness dependent, plays a minor role is consistent with the experimental finding that decay rates are thickness independent for thick nanowires [63].

For thin nanowires, at a certain temperature which is above T_C, the soft mode frequency decreases with thickness due to the depolarization field effect. A thinner nanowire corresponds to a higher soft mode frequency and a smaller dielectric constant, as shown in equation (1.17). Thus, the electric field through a thinner nanowire is larger and accelerates the electron emission. Meanwhile, a higher transverse optical mode frequency results in a faster electron drift mobility. This makes the leakage current and polarization decay constant significantly thickness–dependent for thin wires. For thick nanowires, the soft mode frequency at a certain temperature approaches that of the bulk $BaTiO_3$ crystal. In this range, thickness affects the electric field, electron mobility, and leakage current little. It is worth mentioning that the conclusion, that leakage current depends on thicknesses only for thin nanowires or films, is consistent with previous studies [64, 65, 63].

In this study, the surface adsorbate OH plays the role of top electrode, which is the source of nonequilibrium charge carriers. This modified Schottky model, simulating leakage current in ferroelectric oxides, differs from the traditional Schottky emission model in many aspects. The electrons are localized in a $2p$ orbital, and their wave vector distribution is now not based on Fermi-Dirac statistics. Different from the traditional Schottky emission model, in which the thermal population of electrons leads to the temperature dependence of leakage current, temperature dependent leakage current is attributed to change of electric field through the nanowire and electronic mobility accompanied with the hardening (or softening) of the transverse optical mode in this model.

1.5 Conclusion

In summary, the depolarization process of $BaTiO_3$ nanowires has been studied by both experiment and first principles calculation. We investigated the mechanisms which govern the polarization decay and drew several principles. A new proposed theoretical model, which combines molecular orbital theory, quantum tunneling and the modified Schottky equation, could explain successfully the general trends in the temperature and nanowire thickness dependent decay rates. Our study demonstrates that the surface adsorbate plays a significant role in stabilizing ferroelectricity and that depolarization is a process of charge leaking from the hydroxyl surface adsorbate to the gold substrate.

Chapter 2

Theoretical Modeling of Tribochemical Reaction

2.1 Introduction

Metal oxide semiconductor field effect transistors (MOSFETs) are the fundamental components in electronic logic devices. Moore's law predicts that the number of transistors in a defined size electronic device doubles every two years. Effort toward shrinking the MOSFET scale is always ongoing, but a vital challenge is that the leakage current becomes unacceptably large as the MOSFET size decreases [66]. Besides, the minimum subthreshold swing $S = 60$ meV/decade sets a lower limit for energy dissipation in the MOSFET operation [67, 68]. To overcome these problems, microelectromechanical system (MEMS)

switches are being developed [69, 70, 71, 72, 73]. The source and drain electrodes are separated by an air gap, and they can also be connected by an adjustable conductive bar. Such an electronic device has nearly zero leakage current, and the minimum subthreshold swing also breaks the $S = 60$ meV/decade limitation. However, a prime concern about this approach is the stability of the electrical contact resistance (ECR): a hydrocarbon contaminant forms on the surfaces of the electrodes and on the conductive bar after many switching cycles. This tribopolymer may increase the ECR beyond the tolerance of logic applications [74, 75, 76, 77, 78].

The study of the reliability of MEMS devices has been a fast–moving field [79]. In MEMS devices, Pt and Au are two common electrodes in use. The benefits of using Au electrodes are corrosion retardation, low resistivity, and ease of deposition [80, 81, 82]. However, Au is a soft metal with low cohesive energy, so surface wear and material transfer are the main drawbacks of Au contacts. Also, some contamination can still form after electrical cycling [74, 83]. As for Pt contacts, previous experiments showed that tribopolymer is more prone to form on Pt than on Au. Wabiszewski $et\ al.$ used atomic force microscopy (AFM) to mimic the Pt/Pt electrical contacts. The ECR after cycling was six orders of magnitude higher than before [84]. Brand $et\ al.$ observed considerable amounts of tribopolymer formation on Pt contacts, leading to a dramatic increase of ECR [76, 77].

For Pt contacts, the rate of formation and the amount of tribopolymer are related to how the MEMS switches are operated [76, 77]. Three types of switching-cycle mechanisms are considered in their experimental setup: cold switching, hot switching, and mechanical switching. In cold switching, voltage is applied after the two contacts are closed, and removed before the contacts open. In hot switching, voltage is applied across the device the entire time, whether the contacts are closed or open. In mechanical switching, in order to better understand the role of electrochemistry relative to other effects, the contacts undergo cycles of closing and opening without applying any voltage. When a voltage of 5 V was ap-

plied across the contacts during the cold–switching cycle, a large amount of tribopolymer was generated. However, interestingly, even in mechanical switching, the tribopolymer is still formed, but less compared to the cold switching protocol. In this work, we applied a computational compression experiment to study the effects of mechanical stress and catalysis on tribopolymer formation.

2.2 Methodology

It is believed that the tribopolymer results from the polymerization of hydrocarbon gases from the atmosphere or from packaging. Among them, benzene is the one which causes the most severe contamination [78]. Therefore, benzene is selected as the background gas in our study. In order to investigate tribopolymer formation on Pt contacts in a benzene atmosphere, we conducted compression computational experiments with first–principles density functional theory (DFT) calculations. Au contacts are also studied as a control system to illustrate the tribopolymer formation mechanism. All calculations are performed with the plane–wave DFT package QUANTUM–ESPRESSO [31] using the generalized gradient approximation (GGA) exchange correlation functional. A plane–wave cutoff energy of $E_{\text{cut}} \approx 680$ eV and an $8\times8\times1$ Monkhorst–Pack k–point mesh [34] are used for energy and force calculations. All atoms are represented by norm-conserving pseudopotentials generated by the OPIUM [33] code with a plane-wave cutoff, $\hbar^2 q_c^2/2m_e \approx 680$ eV. The maximum threshold for atomic force convergence is set as 5.0×10^{-3} eV/Å per atom.

A supercell geometry is used with periodically separated metal slabs and two benzene molecules per surface between the slabs to model metal contacts in a benzene atmosphere. A four–layer metal slab is used to simulate top and bottom contacts. Fig. 2.1 shows the initial setup of the supercell structures. The space between the top and bottom contacts is 9.3 Å. The vertical distance between the two parallel benzene molecules is selected to be

4.1 Å, so that the two benzene molecules have little interaction. In the initial structure, the benzene molecules are intact without any deformation. The distance between one benzene molecule and its closest metal contact is 2.6 Å. At this distance, the benzene molecule has an attractive adsorption force toward the contact, and no stress is required to press the molecule to such a position. After the relaxation, the two benzene molecules are strongly chemisorbed on the top and bottom contacts. Once the adsorption system is fully optimized, the value of the distance between each pair of neighboring metal atomic layers, a, is decreased by Δa. Since there are three intervals in the four–layer slabs, the height of the supercell is reduced by $3\Delta a$ in total in each compression step. At the beginning, the value of Δa is selected as 0.2 Å. Once any significant deformation of the adsorbates is observed, we decrease Δa to 0.02 Å or less, in order to have a subtle observation of the structural changes correlated with the height of the supercell. Then, we optimize the compressed system, and after the relaxation, we repeat this compression and optimization process. Our manual adjustment of the supercell is analogous to applying stress to the adsorbed benzene. As the compression process goes on, the normal load (stress) increases. The average stress is calculated from the energy of the system and the dimension of the supercell

$$\sigma = -\frac{1}{S}\frac{\partial E}{\partial z} \tag{2.1}$$

where σ is the stress along the z direction of the system, E is the energy of the system, and S is the area of the surface. Since we have optimized the structure to equilibrium, the stress in the supercell is approximately uniform and the stress on the molecules is the same as the average one.

Energy barriers are calculated with the nudged elastic band (NEB) method implemented in the QUANTUM–ESPRESSO package. The optimization scheme is the quasi–Newton Broyden's second method. Path optimization stops when the norm of the force orthog-

onal to the path is less than 0.05 eV/Å.

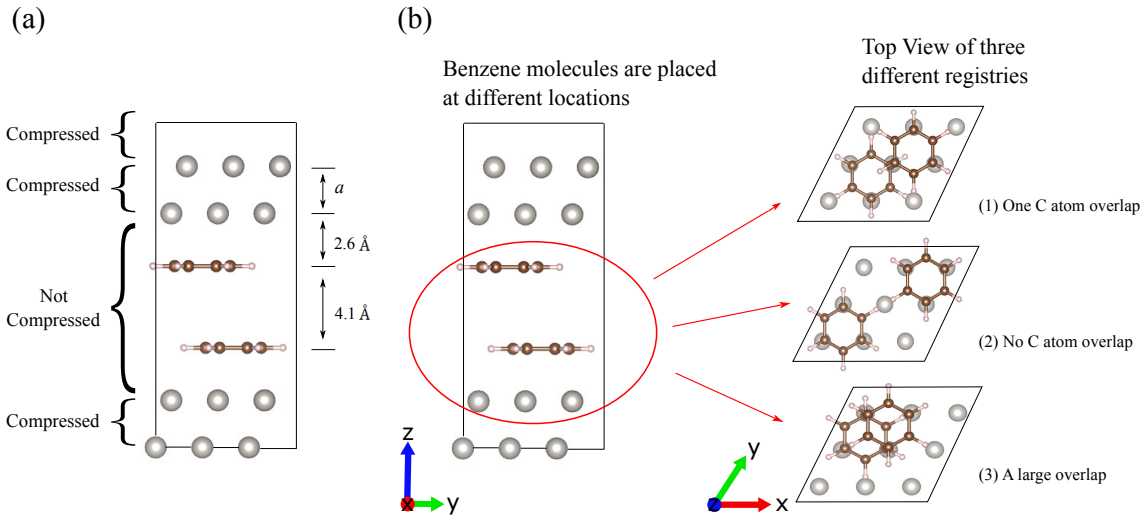

Figure 2.1: Ball–and–stick model of the initial registries of two benzene molecules.

2.3 Results

In Pt–benzene systems, we choose three different registries as shown in Fig. 2.1. In registry (1), there is one carbon atom overlapping between the two benzene molecules from the top view. In the second registry, there is no carbon atom overlap. In registry (3), the two benzene molecules have a relatively large overlap.

During the relaxation, the compressed electrodes will recover to a new equilibrium structure, and hence will expand and squeeze the center vacuum space. The adsorbed molecules at the center will sense the stress applied by the two closing contacts. We conduct compression computational experiments and observe that for all three different registries, when the height of the supercell is reduced to 11.06 Å, chemical reaction occurs: some hydrogen atoms dissociate from the adsorbed benzene molecules, making them less saturated. The carbon atoms which lose their bonded hydrogen atoms form a C–C bond making a biphenyl–like structure, as shown in Fig. 2.2.

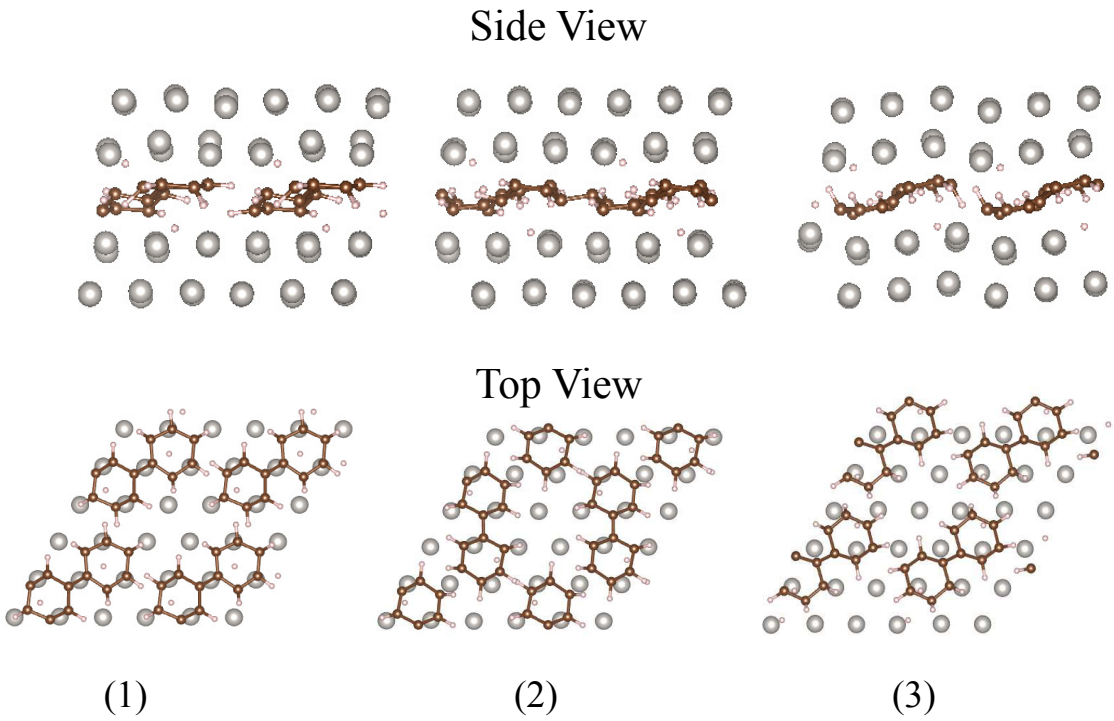

Figure 2.2: Side and top views of the biphenyl–like structure formed after the height of the supercell is reduced to 11.06 Å for the three different registries.

In the following part, we take a more detailed look at the formation of the biphenyl–like structure. For the structure without any compression, the benzene molecules adsorb on the surface and distort to become non–planar. The adsorption is at the hollow site, as it is the most favorable position [85], as shown in Fig. 2.4 (a). The C–C bonds are around 1.5 Å, which is approximately the length of C–C single bond. These indicate the chemisorption of benzene on Pt(111) surface. The bonding between C and Pt induces the H atoms to move away from the surface, indicating sp^3 C character. The C–Pt bond distances are approximately 2.1 Å. We should also note that before the compression (no external stress applied), the distance between one H atom and its closest Pt atom is approximately 2.7 Å, which is much larger than the length of a Pt–H bond (1.7 Å) [86]. There is no chemical bond between Pt and H atoms.

Taking the first registry as an example, the changes of the structure with the height of

the supercell c and the resulting σ are shown in Fig. 2.3. When the stress increases to 24.0 GPa, it can been seen that one H atom is pushed close to a Pt atom, as shown in Fig. 2.4 (b).

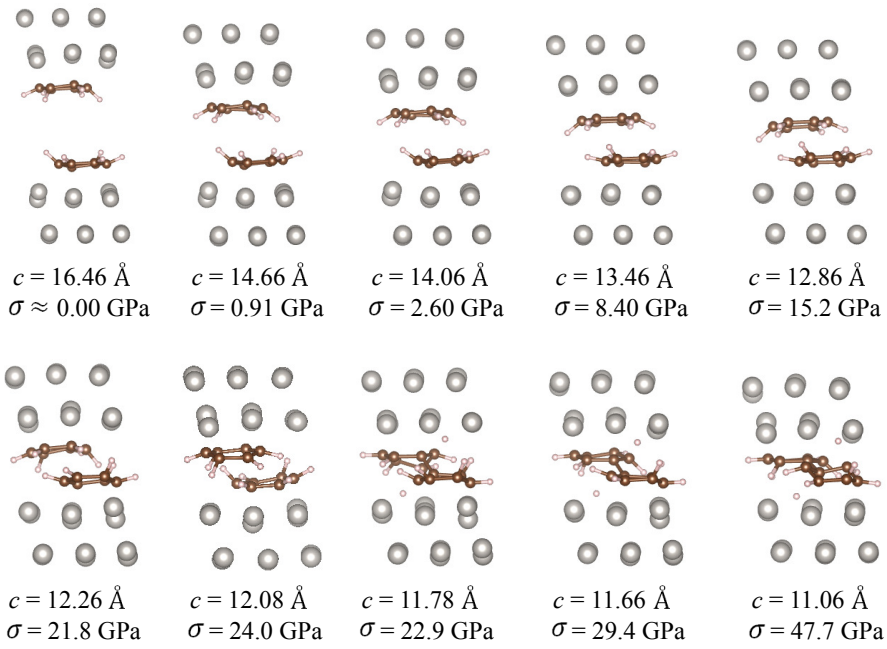

Figure 2.3: Ball–and–stick model of the entire compression process of the supercell with benzene on the Pt(111) surface.

As we compress the system further, a C–H bond breaks, and the H atom is attached to the Pt substrate, as shown in Fig. 2.4 (c). The adsorption position of the dissociated H atom is the hollow site, which is the most stable one [87]. Two C atoms which lose their H atoms form a C–C bond, and connecting the carbon rings builds a biphenyl–like structure, as shown in FIG. 2.4 (d). The adsorbed benzene molecules are on the way to more dramatic change: (1) H atoms can fall off due to further compression. The detached atoms may form H_2 and escape into the atmosphere, which indicates that the dehydrogenation is a non–reversible process; (2) C atoms which lose their H atoms become less saturated and more reactive. As these processes continue, more hydrogen atoms may fall off, and reactive C atoms link with others or even pile up, forming a two dimensional or three dimensional

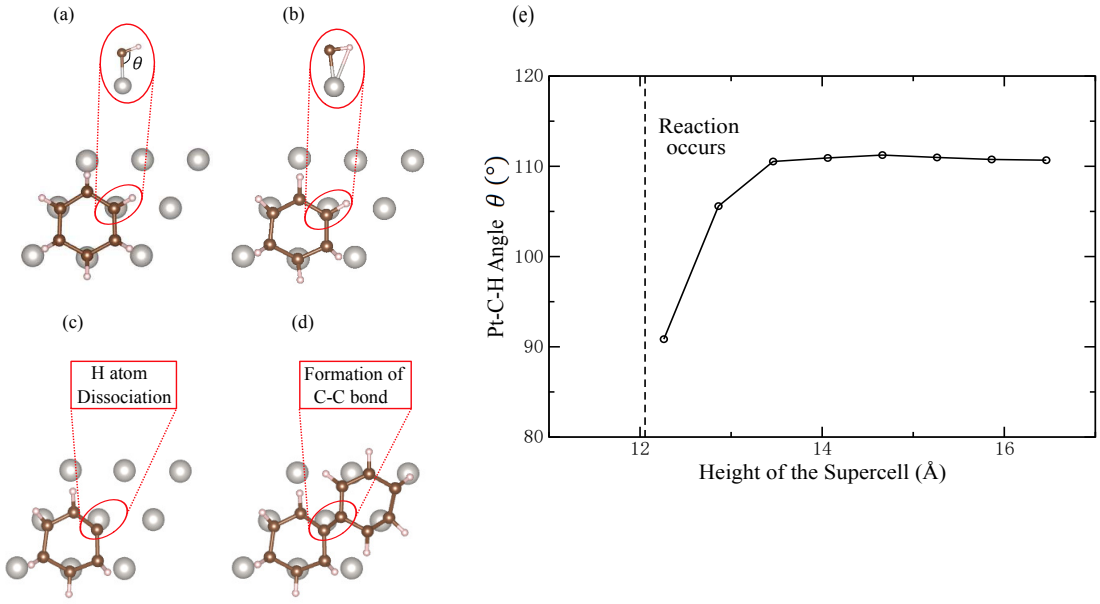

Figure 2.4: (a-d) Ball–and–stick model of detailed benzene bonding geometry and reactivity on Pt (111). (e) The plot of supercell height $vs.$ the Pt–C–H angle.

C–rich network. The biphenyl–like linked rings (Fig. 2.4) can be viewed as the primary step of tribopolymer formation.

To further investigate the dehydrogenation and polymerization processes, we use the NEB [88] method to calculate the energy barrier at different unit cell heights, as shown in Fig. 2.5. Energies of the structures without polymer formation are shown in red, whereas the black points correspond to the polymerized structures. The subplot shows the detailed stress effect on the polymer formation process. With mechanical load applied, structure ① evolves to ②, which is the structure one step before the formation of polymer. The energy drops to ③, indicating the polymer formation. Continued compression of the cell does not lead to additional new species formation. ④ is an expansion step back up to the same supercell volume as ②. Further expansion changes the structure to ⑤;

Initial structures with different supercell heights provide different stress/mechanical loads. The calculated unit cell height dependence of reaction energies is shown in Fig. 2.6 (a). For stress below 24.22 GPa, there is a linear relation between stress and reaction

barrier, which is consistent with a Brønsted–Evans–Polanyi (BEP) relationship [89, 90, 91] as expressed

$$\Delta E_{\mathrm{act}} = \alpha \Delta H = \alpha F \cdot \Delta d \tag{2.2}$$

where ΔE_{act} is the change of activation energy E_{act}, α $(0 \leq \alpha \leq 1)$ is a constant which characterizes the position of the transition state, H is the enthalpy of the reaction, F is the applied force, which is proportional to the stress, and Δd is the distance that the force F moves though along the reaction coordinate. As we increase the stress and the dimension of the system shrinks by Δd, a work

$$W = F \cdot \Delta d \tag{2.3}$$

is applied to the system. This energy is added to the adsorbates, promoting the reaction, as shown in Fig. 2.5 (b). If the stress increases further, the energy barrier drops to zero within just a 0.2 GPa period, as in Fig. 2.6 (a) and (b). This breakdown of the BEP relationship is attributed to the catalysis effect of Pt. Compression not only adds energy to the adsorbates, but also presses hydrogen atoms close to the Pt substrate, changing the reaction pathway. Pt, as a catalyst, can weaken the C–H bond and reduce the reaction energy barrier [92, 93, 94]. The stronger the Pt–H interaction is, the lower the energy barrier is.

The reaction occurs when the stress is 24.42 GPa. In the following part, we demonstrate that the threshold stress can be reduced by including the electrochemical effect. Above 24.22 GPa, the relationship of the supercell height and energy barrier deviates from linearity. We deduce that from this point, Pt begins to affect the dehydrogenation as a catalyst. The chemical reaction can be expressed as

$$\mathrm{C_6H_6} \;\rightarrow\; \mathrm{C_6H_5}\cdot \;+\; \left(\mathrm{H^+ + e^-}\right). \tag{2.4}$$

And the reaction energy change due to applied potential U is [95]

$$\Delta E^{*}_{\mathrm{act}} = \Delta E_{\mathrm{act}} - n \cdot e \cdot U \tag{2.5}$$

where e is the electron charge and n is the number of electrons involved in the reaction. At 24.22 GPa, the energy barrier is 0.051 eV, and in experiments, the applied voltage (5.0 V) during device switching is larger than 0.051 V. Therefore, due to the electrochemical effect, the H atom can get one electron and leave the benzene as soon as it makes electrical contact with the electrode.

The process of adsorbed benzene molecules losing H atoms and linking together by C bonds can be summarized as: (1) benzene molecules are adsorbed on the Pt surfaces; (2) due to the closure of the Pt contacts, stress is applied to the adsorbate, flattening it and making C–H bonds easier to break. We emphasize that while the H atoms are not close to the Pt substrate, the fragility of adsorbed benzene mainly results from mechanical load (rather than catalytic effect), and the activation energy–stress relationship obeys the BEP relationship; (3) As the stress increases further, the benzene adsorbates become flat enough and the H atoms begin to be attracted to the Pt atoms. Pt weakens the C–H bond and accelerates the dehydrogenation process, as shown in Fig. 2.5 (b). This effect can also be enhanced by electrochemistry.

In the following section, computational compression experiments of a Au–benzene system are analyzed as a contrast with Pt, highlighting the importance of adsorption and catalysis in polymerization. In Fig. 2.7, the changes of the Au–benzene structure during the compression are shown. At the outset, benzene molecules are not strongly adsorbed on the contact surfaces, with a -0.1 eV adsorption energy, much weaker than on Pt (-1.9 eV). After normal load is applied, benzene molecules spontaneously glide and avoid each other, due to the lack of strong adsorption or fixed location. As the compression increases, the benzene

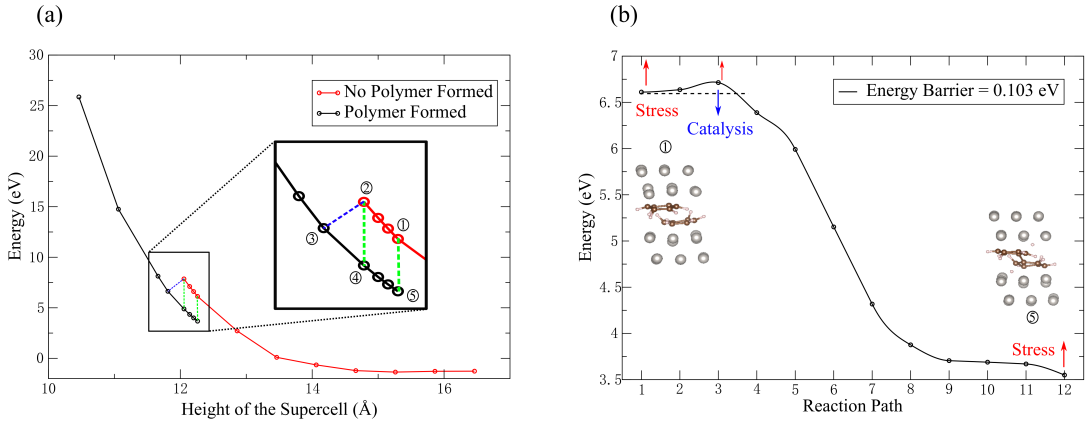

Figure 2.5: Energetic behavior of the compression process.

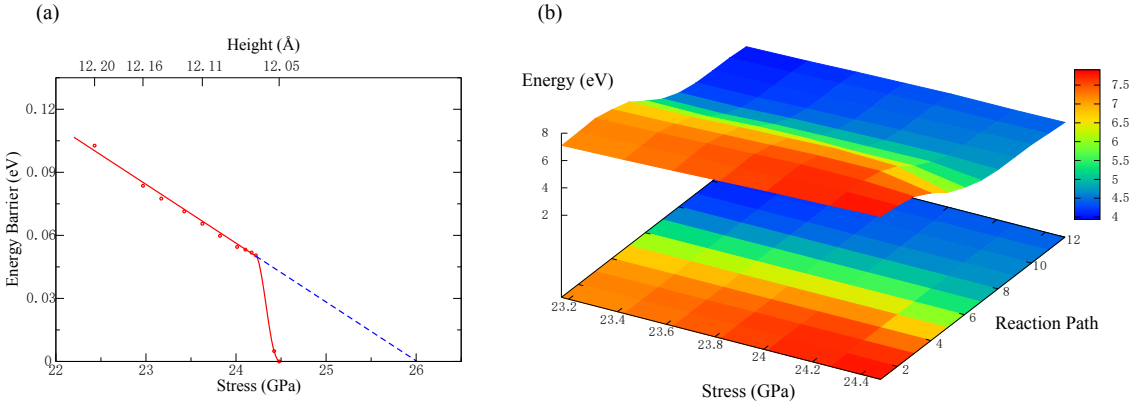

Figure 2.6: (a) Energy barriers for benzene on Pt at different stresses. (b) The change of reaction paths with applied stress.

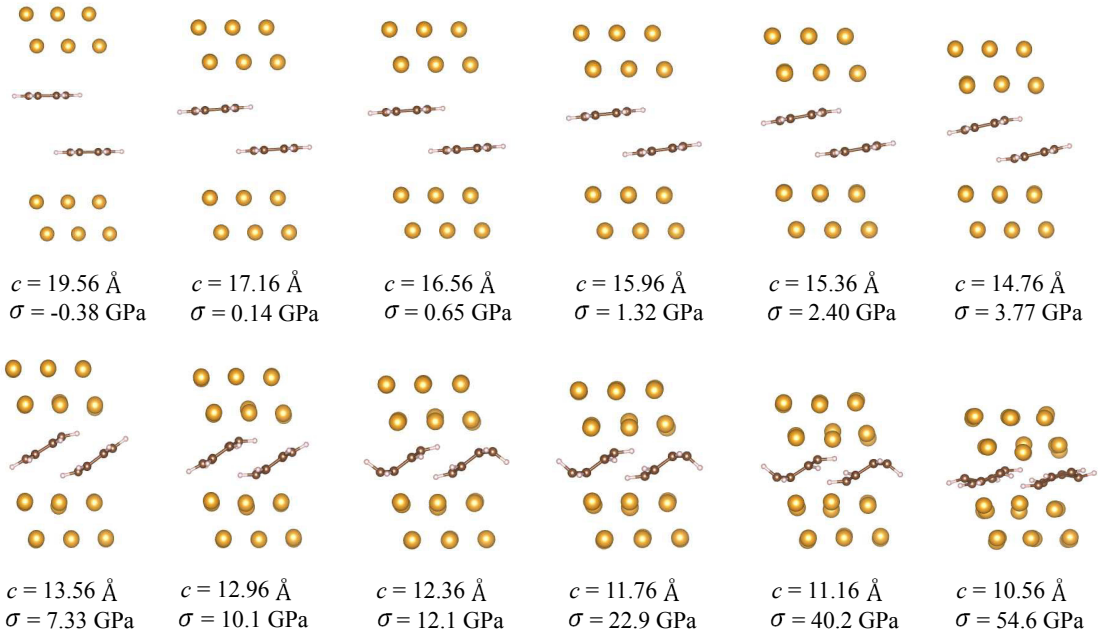

Figure 2.7: Ball–and–stick model of the compression of benzene on the Au(111) surface. No polymer formation is seen during the compression.

molecules begin to distort, because of the reduction of free space and applied stress. Different from the benzene on Pt contacts case, there is no C–H bonds broken. Even though the benzene ring is broken at the high stress cases and Au–C bonds are able to form, no polymerization is observed, even when the height of the supercell is reduced to 10.56 Å with stress of 54.6 GPa, which is far beyond the requirement of benzene polymerization on Pt contacts ($\approx$ 24 GPa).

As we know, Au is the noblest metal, possessing a completely filled d–band, and the d–band center is far from the Fermi level [96]. As a result, the bonds that form between Au and adsorbates have anti–bonding orbitals that are partially or mostly filled, indicating that the bonding itself is not stable. Therefore, Au contacts cannot adsorb molecules tightly, so there is nothing to stop intermolecular gliding, and Au does not catalyze the dehydrogenation reaction.

If the concentration of benzene is low, the molecules tend to escape from the center

space between the two Au contacts, making tribopolymer formation less likely. For the high concentration case, if lots of benzene molecules are trapped in a certain region during the switching, the mechanical load can eventually induce the polymerization. Previous theoretical study demonstrates that benzene molecules can transform to a polymeric phase due solely to pressure [97], but the required polymerization pressure is relatively high, above 80 GPa.

The main differences between the Pt and Au cases are the adsorption and dehydrogenation. Adsorption is important, because it not only prevents the repulsion and avoidance of molecules, but also breaks the strong and stable delocalized π orbital. For the Au contacts with little adsorption, the delocalized π system is crushed only by the mechanical load, and there is a stricter requirement for this process, such as a higher molecule concentration or larger mechanical load. However, for the polymerization on Pt case, the strong delocalized π system is broken by the adsorption onto the substrate. Polymerization is induced by the breaking of the C–H bonds, and this process is much easier.

For Pt contacts, computational compression experiments demonstrate that polymerization can occur under stress of 24.22 GPa. Compared with the pure benzene polymerization stress 80 GPa, it is much closer to the experimental situation, for which the stress between contacts is estimated at several GPa. Besides, only uniaxial stress is investigated in this study. Shear may also assist the dehydrogenation, accelerate the polymerization, and hence lower the polymerization threshold stress. Moreover, in the study, a flat Pt surface is assumed. Steps and vacancies can also enhance the catalysis effect and reduce the threshold polymerization stress.

2.4 Conclusion

In this study, the mechanism of tribopolymer formation has been studied by computational compression experiments. Benzene molecules adsorb on the surfaces of contacts, and then original chemical bonds can be broken due to mechanical load. Dehydrogenation makes adsorbed benzene molecules less saturated, so they bond with others to form tribopolymer. In a certain stress range, the reaction energy decreases with mechanical load, and the linear relationship between E_{act} and P follows the BEP relationship. When the stress is large enough to press H atoms close to the Pt substrate, a catalytic effect takes over and the energy barrier decreases to zero more rapidly as stress increases. Our study provides a detailed analysis of the process and mechanism of the initial stage of tribopolymer formation on contacts in MEMS and NEMS.

Chapter 3

Atomistic Description for Temperature–Driven Phase Transitions in $BaTiO_3$

DOI: https://doi.org/10.1103/PhysRevB.94.134308

3.1 Introduction

$BaTiO_3$ is a ferroelectric perovskite with promising applications in electronic devices, such as non–volatile memory, high–κ dielectrics, and piezoelectric sensors [6, 98, 99, 100]. Therefore, it is of great significance to investigate and understand the structural and elec-

tronic properties of $BaTiO_3$ for designed material optimization and device engineering. First–principles density functional theory (DFT) has served as a powerful method to understand the electronic structures of ferroelectric materials [101, 102, 103, 15, 104, 105]. Due to the expensive computational cost, the application of DFT methods is currently limited to system of fairly small size at zero Kelvin. Many important dynamical properties, such as domain wall motions and temperature–driven phase transitions, are beyond the capability of conventional first–principles methods. An effective Hamiltonian method was developed to study finite–temperature properties of $BaTiO_3$ [106, 107, 108, 109]. To apply this method, the subset of dynamical modes that determine a specific property should be known *a priori*. Molecular dynamics (MD) simulations with an atomistic potential accounting for all the modes offer distinct advantages, especially in providing detailed information about atomic positions, velocities and modifications of chemical bonds due to a chemical reaction or thermal excitation. The shell model for $BaTiO_3$ has been developed [110, 111, 112, 113, 114]. However, due to the low mass assigned to the shell, a small time step in MD simulations is required to achieve accurate results, which limits the time and length scales of the simulations.

Recently, we developed a bond–valence (BV) model potential for oxides based on the bond valence theory [115, 116, 117, 118, 119]. The force fields for many technologically important ferroelectric materials, $PbTiO_3$, $PbZrO_3$ and $BiFeO_3$ [118, 119, 117, 115, 120], have been parameterized based on results from DFT calculations. A typical force field requires no more than 15 parameters and can be efficiently implemented, which enables simulations of systems with thousands of atoms under periodic boundary conditions [121, 122]. The development of an accurate classical potential for $BaTiO_3$ has proven to be difficult, mainly due to the small energy differences among the four phases (rhombohedral, orthorhombic, tetragonal, and cubic) [123, 124, 125]. In this paper,

we apply the bond–valence model to $BaTiO_3$ and parameterize the all–atom interatomic potential to first–principles data. Our model potential for $BaTiO_3$ is able to reproduce the rhombohedral–orthorhombic–tetragonal–cubic (R-O-T-C) phase transition sequence in isobaric–isothermal ensemble (NPT) MD simulations. The phase transition temperatures agree reasonably well with previous theoretical results [110]. We further examine the temperature dependence of the local displacements of Ti atoms and discover several features of the phase transitions of $BaTiO_3$: the phase transitions of $BaTiO_3$ involve both order–disorder and displacive characters; at the moment that the phase transition of the crystal occurs, all the polarization components undergo phase transitions, even for the nonpolar ones; and temperature increase can also cause bond–hardening for a certain component.

3.2 Methods

The bond–valence model potential is developed based on the conservation principles of bond valence and bond–valence vector. The bond valence, V_{ij}, reflects the bonding strength and can be calculated based on the bond length, r_{ij}, with [126, 115, 127, 128, 118, 119, 116, 117]

$$V_{ij} = \left(\frac{r_{0,ij}}{r_{ij}} \right)^{C_{ij}} \tag{3.1}$$

where i and j are the labels for atoms; $r_{0,ij}$ and C_{ij} are Brown's empirical parameters. The bond–valence vector is defined as a vector lying along the bond, $\mathbf{V}_{ij} = V_{ij}\hat{\mathbf{R}}_{ij}$, where $\hat{\mathbf{R}}_{ij}$ is the unit vector pointing from atom i to atom j. The total energy (E) consists of the Coulombic energy (E_c), the short–range repulsive energy (E_r), the bond–valence energy (E_{BV}), the bond–valence vector energy (E_{BVV}), and the angle potential (E_a) [118, 119, 116, 117]:

$$E = E_c + E_r + E_{\mathrm{BV}} + E_{\mathrm{BVV}} + E_a \tag{3.2}$$

$$E_c = \sum_{i<j} \frac{q_i q_j}{r_{ij}}, \tag{3.3}$$

$$E_r = \sum_{i<j} \left(\frac{B_{ij}}{r_{ij}} \right)^{12}, \tag{3.4}$$

$$E_{\mathrm{BV}} = \sum_i S_i \left(V_i - V_{0,i} \right)^2 \tag{3.5}$$

$$E_{\mathrm{BVV}} = \sum_i D_i \left(\mathbf{W}_i^2 - \mathbf{W}_{0,i}^2 \right)^2 \tag{3.6}$$

$$E_a = k \sum_i^{N_{\mathrm{oxygen}}} \left(\theta_i - 180^\circ \right)^2 \tag{3.7}$$

where $V_i = \sum_{j \neq i} V_{ij}$ is the bond–valence sum (BVS), $\mathbf{W}_i = \sum_{j \neq i} \mathbf{V}_{ij}$ is the bond–valence vector sum (BVVS, shown in Fig. 3.1 (a), (b)), q_i is the ionic charge, B_{ij} is the short–range repulsion parameter, S_i and D_i are scaling parameters with the unit of energy, k is the spring constant and θ is the O–O–O angle along the common axis of two adjacent oxygen octahedra (Fig. 3.1 (c)). The bond-valence energy E_{BV} captures the energy penalty for both overbonded and underbonded atoms. The bond-valence vector energy E_{BVV} is a measure of the breaking of local symmetry, which is important for correctly describing the ferroelectricity. $V_{0,i}$ and $\mathbf{W}_{0,i}$ are preferred or target values of BVS and BVVS for atom i in the ground–state structure, which can be calculated from DFT directly. It is noted that the E_{BV} and E_{BVV} can be related to the moments of the local density of states in the framework of a tight binding model, providing a quantum mechanical justification for these two energy terms [118, 119, 129, 126, 130]. The angle potential is used to account for the energy cost associated with the rotations of oxygen octahedra.

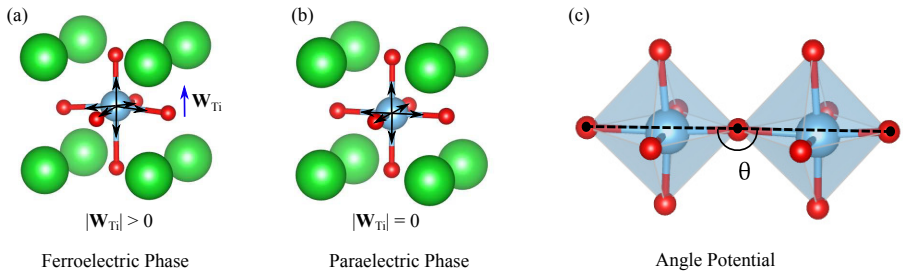

Figure 3.1: Bond valence vector sum and angle potential.

We followed the optimization protocol developed in previous studies [118, 119]. The optimal values of force-field parameters q_i, S_i, D_i and B_{ij}, are acquired by minimizing the difference between the DFT energies/forces and the model–potential energies/forces for a database of $BaTiO_3$ structures. All DFT calculations are carried out with the plane–wave DFT package QUANTUM–ESPRESSO [31] using the Perdew–Burke–Ernzerhof functional modified for solids (PBEsol) [131] and optimized norm–conserving pseudopotentials generated by the OPIUM package [33]. A plane–wave cutoff energy of 50 Ry and $4\times4\times4$ Monkhorst–Pack k–point mesh [34] are used for energy and force calcualtions. The database consists of 40–atom $2\times2\times2$ supercells with different lattice constants and local ion displacements. The final average difference between DFT energy and model–potential energy is 1.35 meV/atom.

3.3 Performance of the classical potential

The optimized parameters are listed in Table 3.1. The performance of the obtained force field is examined by investigating the temperature dependence of lattice constants (a, b and c), component–resolved local displacements of Ti atoms (d_x, d_y, and d_z), and the three components of the total polarization (P_x, P_y, and P_z). We carried out NPT MD simulations using a $10\times10\times10$ supercell (5000 atoms) with the temperature controlled via the Nosé–Hoover thermostat and the pressure maintained at 1 atm via the Parrinello–Rahman

	$r_{0,\beta\mathrm{O}}$	$C_{0,\beta\mathrm{O}}$	q_β(e)	S_β(eV)	D_β
Ba	2.290	8.94	1.34730	0.59739	0.08429
Ti	1.798	5.20	1.28905	0.16533	0.82484
O			-0.87878	0.93063	0.28006

	$B_{\beta\beta'}$ (Å)				
	Ba	Ti	O	$V_{0,\beta}$	$\mathbf{W}_{0,\beta}$
Ba	2.44805	2.32592	1.98792	2.0	0.11561
Ti		2.73825	1.37741	4.0	0.39437
O			1.99269	2.0	0.31651

Table 3.1: Optimized force field for $BaTiO_3$. The angle constant $k = 6.1$ meV/(deg)^2.

barostat [132]. Each simulation was performed for 80 ps with a 1 fs time step. The thermal inertia parameter M_s was selected as 1.0 for the first 20 ps and 5.0 for the rest 60 ps. The local polarization of each unit cell $\boldsymbol{P_u}(t)$ is expressed as

$$\boldsymbol{P_u}(t) = \frac{1}{V_u}\left(\frac{1}{8}\boldsymbol{Z}^*_{\mathrm{Ba}}\sum_{i=1}^{8}\boldsymbol{r}_{\mathrm{Ba,i}}(t) + \boldsymbol{Z}^*_{\mathrm{Ti}}\boldsymbol{r}_{\mathrm{Ti,i}}(t) + \frac{1}{2}\boldsymbol{Z}^*_{\mathrm{O}}\sum_{i=1}^{6}\boldsymbol{r}_{\mathrm{O,i}}(t)\right) \tag{3.8}$$

where V_u is the volume of a unit cell, $\boldsymbol{Z}^*_{\mathrm{Ba}}$, $\boldsymbol{Z}^*_{\mathrm{Ti}}$, and $\boldsymbol{Z}^*_{\mathrm{O}}$ are the Born effective charges of Ba, Ti, and O atoms, with $\boldsymbol{Z}^*_{\mathrm{Ba}} = 2.9$, $\boldsymbol{Z}^*_{\mathrm{Ti}} = 6.7$, and $\boldsymbol{Z}^*_{\mathrm{O}} = \frac{1}{3}\left(\boldsymbol{Z}^*_{\mathrm{Ba}} + \boldsymbol{Z}^*_{\mathrm{Ti}}\right)$ [133]. $\boldsymbol{r}_{\mathrm{Ba,i}}(t)$, $\boldsymbol{r}_{\mathrm{Ti,i}}(t)$, and $\boldsymbol{r}_{\mathrm{O,i}}(t)$ are the positions of Ba, Ti, and O atoms at time t.

As shown in Fig. 3.2, the simulations clearly reveal four distinct phases under different temperature ranges and three first–order phase transitions. Below 100 K, the displacements of Ti atoms and the overall polarization of the supercell are along [111] direction ($P_x = P_y = P_z$), characteristic of the rhombohedral phase. At 100 K, the z component of the total polarization, P_z, becomes approximately 0, indicating a phase transition from rhombohedral to orthorhombic ($P_x = P_y > 0$, $P_z = 0$). As the temperature increases further to 110 K, the total polarization aligns preferentially along x direction ($P_x > 0$, $P_y = P_z = 0$) and the lattice constants have $b = c < a$. The supercell stays tetragonal until

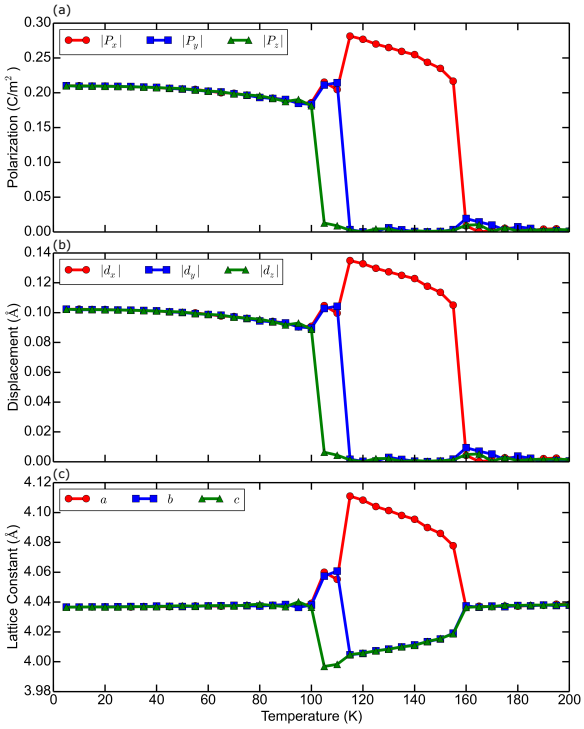

Figure 3.2: Temperature dependence of the polarization, Ti displacement, and lattice constants in $BaTiO_3$.

	R–O	O–T	T–C
BV model	100 K	110 K	160 K
Shell model	80 K	120 K	170 K
Experiments	183 K	278 K	393 K

Table 3.2: Comparison of the phase transition temperatures given by the BV model, the shell model, and experiments.

160 K at which point the ferroelectric–paraelectric phase transition occurs. The phase transition temperatures match well with those predicted by the shell model [110] (Table 3.2). Experimental phase transition temperatures [134] are also listed in Table 3.2. It can be seen that phase transition temperatures are consistently underestimated in our MD simulations. This underestimation has been observed previously in other DFT fitted simulations, and is due to the systematic error of exchange–correlation functional used for force field optimization [118, 107, 135, 134]. The accuracy of DFT depends on exchange–correlation functionals. Using different exchange–correlation functionals in parameterization affects the simulated phase transition temperatures, but nearly all DFT calculations underestimate the energy barries between states corresponding to different phases [134]. There are ad–hoc techniques for fixing this problem, such as scaling the ab–initio energy surface [134] or using a negative pressure [107]. These techniques would not be discussed detailedly in this study, because the underestimation does not affect the practiacl application of this potential much [118, 119, 120, 122]. We extract the averaged lattice constants at finite temperatures from MD simulations and find that they are in good agreement (error less than 1%) with the PBEsol values (Table 3.3).

Domain walls are interfaces separating domains with different polarities. They are important topological defects and can be moved by applying external stimulus [121, 122]. The domain wall energy for a 180° wall obtained from our MD simulations is 6.63 mJ/m^2, which is comparable to PBEsol value, 7.84 mJ/m^2. This indicates that our atomistic po-

Lattice constant	MD (Å)	DFT (Å)	error
Rhombohedral			
$a = b = c$	4.036	4.024	0.30%
Orthorhombic			
a	3.997	3.977	0.50%
$b = c$	4.059	4.046	0.32%
Tetragonal			
$a = b$	4.005	3.985	0.50%
c	4.109	4.089	0.49%
Cubic			
$a = b = c$	4.037	4.002	0.87%

Table 3.3: Comparison of lattice constants of $BaTiO_3$ given by MD simulations with BV model potential and PBEsol DFT calculations. For MD simulation, lattice constants of rhombohedral, orthorhombic, tetragonal and cubic phases are obtained at 5 K, 105 K, 120 K and 165 K respectively.

tential can be used for studying the dynamics of ferroelectric domain walls in $BaTiO_3$. All these results demonstrate the robustness of this developed classical potential. This potentail is an atomistic potential, in which modeled atoms represent real atoms. By using this potential, we can calculate real experimental observables, such as dielectric constant, frequency dependent dielectric response, vibrational modes, and their temperature, pressure and stress dependence. In the following section, we will discuss atomistic features of $BaTiO_3$ phase transitions.

3.4 Atomistic features of different phases

To provide an atomistic description of the different phases of $BaTiO_3$, we analyze the distribution of local displacements of Ti atoms in each phase. Ti displacement is defined as the distance between the Ti atom and the center of the oxygen octahedral cage of a unit cell, which scales with the magnitude of polarization.

In FIG. 3.3 (a), we plot the distributions of Ti displacements ($d = \sqrt{d_x^2 + d_y^2 + d_z^2}$).

It can be seen that in all four phases, the distribution is approximately a Gaussian curve whose peak shifts toward lower values as the temperature increases. This suggests that the temperature–driven phase transition has a displacive character. It is noted that the distribution of magnitudes is peaked at non–zero value even in the paraelectric cubic phase, suggesting that most Ti atoms are still locally displaced at high temperature, and that the overall net zero polarization is the result of an isotropic distribution of local dipoles along different directions. This confirms the order–disorder character for $BaTiO_3$ at high temperature.

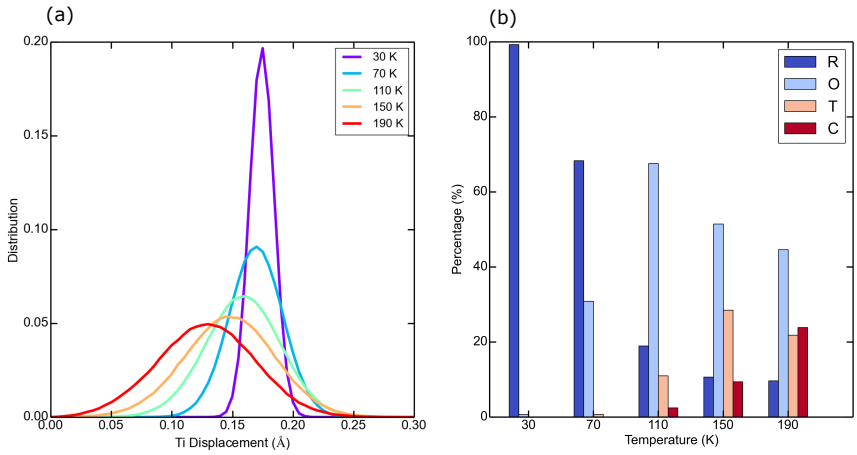

Figure 3.3: (a) The distribution of total Ti displacement magnitude at different temperatures. (b) Instantaneous compositions of different phases.

We can categorize the instantaneous phase of each unit cell based on the local displacement of Ti atom. The categorization criteria are

(1) If $d < 0.1$ Å, the unit cell is considered to be paraelectric cubic;

(2) For a ferroelectric unit cell, the k–th component is considered to be ferroelectric if $d_k > d/\sqrt{6}$. The rhombohedral, orthorhombic, and tetragonal unit cells have three, two, and one ferroelectric component(s), respectively.

The results are shown in FIG. 3.3 (b). At 30 K, the supercell is made only from rhombohedral unit cells, showing that the rhombohedral phase is the ground–state structure. As

	Rhombohedral	Orthorhombic	Tetragonal	Cubic
Energy (meV/unit cell)	-39.31	-37.23	-29.47	0

Table 3.4: Relative energies (potential energies) of different phases from DFT calculations. The cubic unit cell is chosen as the reference structure.

the temperature increases, the supercell becomes a mixture of the four phases. It should be noted that the cubic unit cell with nearly–zero local Ti displacement seldom appears, because a cubic unit cell is energetically less favorable. The relative energies of the four phases of $BaTiO_3$ from PBEsol DFT calculations are listed in Table 3.4. It can be seen that the energy differences between the tetragonal, orthorhombic and rhombohedral unit cells are small (within several meV per unit cell) [136, 101]. Due to the thermal fluctuations, the populations of higher–energy ferroelectric phases (tetragonal and orthorhombic) increase as temperature increases. Above the ferroelectric–paraelectric transition temperature, locally ferroelectric unit cells are still favored over paraelectric due to the relatively high energy of cubic, the high–symmetry structure.

In Fig. 3.4, the distributions of Ti displacements along the three axes are plotted. At 100 K, $BaTiO_3$ is at the rhombohedral phase and the distributions of Ti displacements are Gaussian–like. As the temperature increases, the phase changes to orthorhombic. The average of the x polarization component shifts to zero, indicating a displacive phase transition. Besides, the standard deviation increases and the center of the distribution curve becomes flatter. For the cubic phase, the center of the Ti displacement distribution curve is also flat. As shown in Fig. 3.5, the center–flat curve is a summation of a Gaussian curve centering at zero, and a double–peak curve. The latter is characteristic of order–disorder transition [121]. These results further demonstrate that phase transitions of $BaTiO_3$ have a mix of order–disorder and displacive characters [137, 138, 139, 140, 141, 142, 123].

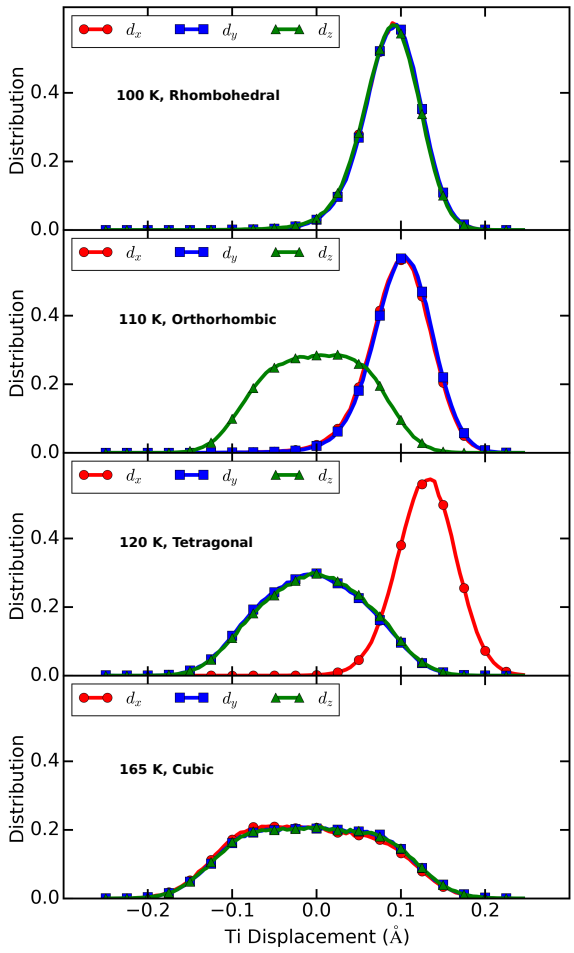

Figure 3.4: The distributions of Ti displacement at different temperatures.

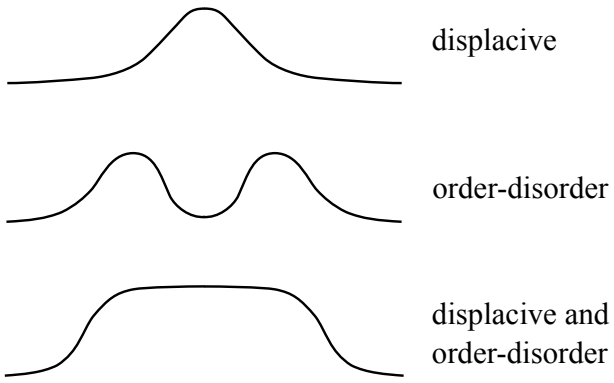

Figure 3.5: Schematic figure of the distributions of Ti displacement for displacive transition, order–disorder transition and a mix of them.

3.5 Features of the phase transitions

To investigate the structural dynamics during phase transitions in more detail, we conducted MD simulations with varying temperatures. In three different sets of simulations, the temperatures were increased from 100 K to 110 K (R to O), 110 K to 120 K (O to T) and 155 K to 165 K (T to C) respectively. The temperature was controlled by the Nosé–Hoover thermostat with a thermal inertia parameter M_s=10 and the 10 K temperature change was accomplished in 60 ps. We analyze the temperature dependence of Ti displacement distributions along three axes. The dynamics of Ti displacement distributions during the phase transitions are plotted in Fig. 3.6. The time evolution of the average and standard deviation of the Ti displacement distributions are shown in Fig. 3.7.

Phase transition occurs when one component undergoes polar–nonpolar transition. The first column (from 100 K to 110 K) shows the changes of Ti displacement distributions during the rhombohedral to orthorhombic phase transition. In the x and y direction, the averages of the distribution shift up, which is a characteristic of displacive transition. Meanwhile, in the z direction, the average becomes zero and the variance becomes significantly larger, indicating that the transition is a mix of displacive and bond–softening characters [143]. For the orthorhombic to tetragonal phase transition (second column),

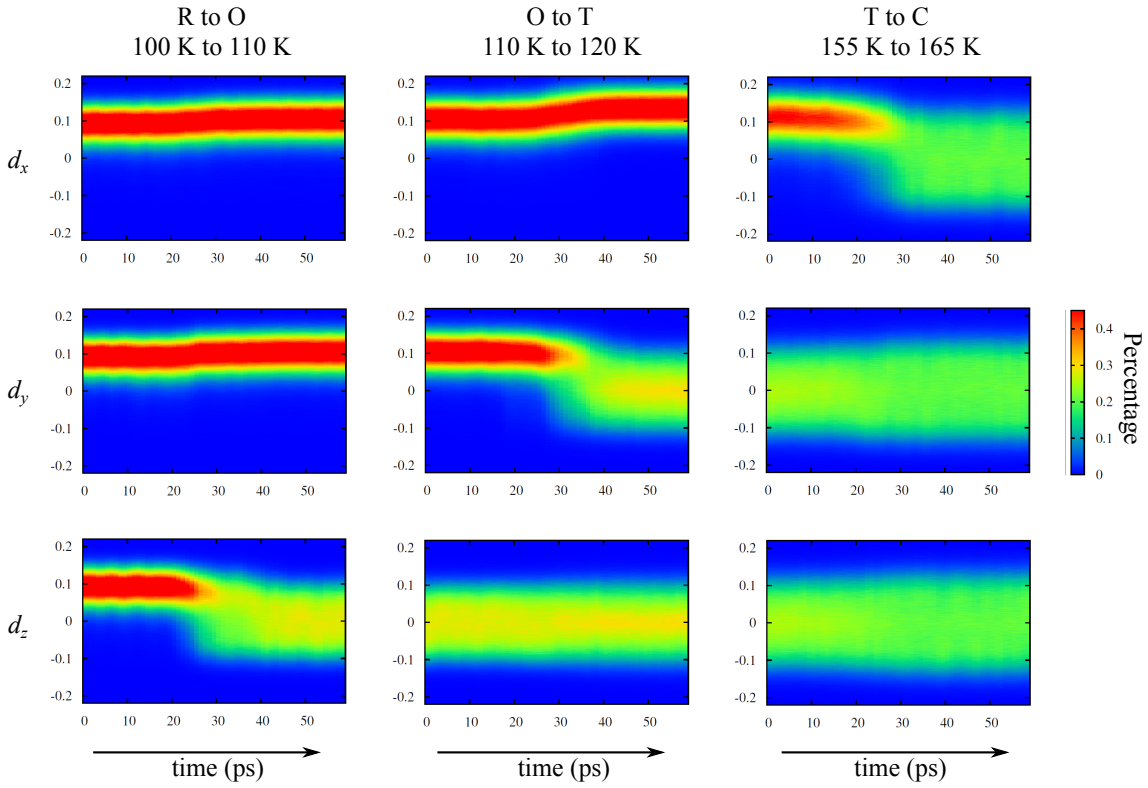

Figure 3.6: Temperature dependence of Ti displacement distributions in three Cartesian directions. The color scale represents the percentages of Ti displacement with a certain value.

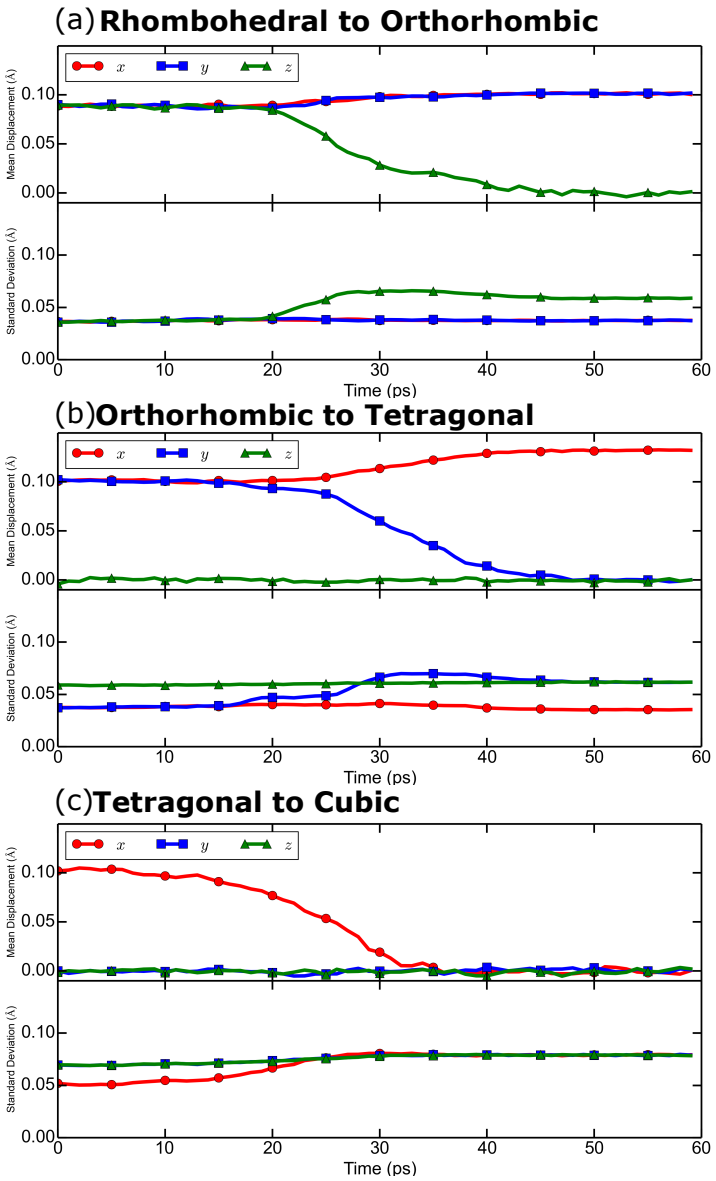

Figure 3.7: The change of the average and standard deviation of the Ti displacement distribution. In the standard deviation plot of (b), the green and black lines increase with temperature and are parallel until the transition.

the transition of the y component, which is a polar–nonpolar transition, includes both displacive and bond–softening features. For the x component, the transition involves both an increase of the average and a decrease of the standard deviation. For the z direction, even though the Ti displacement distribution is centered at zero above and below the transition, the Ti displacements are located closer to zero, indicating an increase in bond hardness. From 155 K to 165 K, there is also a bond–hardness–changing transition for the components (x and y) with zero averages. We collectively refer to 'bond–softening' and 'bond–hardening' as 'bond–hardness–changing'.

Based on the features of the Ti displacement distributions at different phases, the schematic representation of the thermal excitation between different energy surfaces is presented in Fig. 3.8. There are two points worth mentioning: (1) For the x component (first column), the minima of the energy profile for the tetragonal phase are further from the center and have a higher curvature, compared with those for orthorhombic phase, because the Ti displacement distribution has a larger average and smaller variance; (2) For the z component (third column), compared with the energy profile for orthorhombic phase, the one for the tetragonal phase has a higher curvature at the center (Ti displacement more closely distributed around 0, as seen from Fig. 3.6) and smaller curvature for larger z–direction displacements (larger standard deviation, seen from Fig. 3.7 (b).

From our results, the characteristics of $BaTiO_3$ phase transition can be summarized as: (1) For $BaTiO_3$, the mechanisms of phase transitions include both bond–hardness–changing and displacive transition. The sudden shifts of the average and standard deviation correspond to displacive with some order–disorder contribution and bond–hardness–changing transitions respectively; (2) Unlike the conventional understanding that thermal excitation usually causes bond–softening, increasing temperature can also cause bond hardening. The x component of polarization during the orthorhombic to tetragonal transition is an example of this case. (3) When the phase transition occurs, each component of polarization un-

	R to O			O to T			T to C		
Component	d_x	d_y	d_z	d_x	d_y	d_z	d_x	d_y	d_z
Hardness–changing	N	N	Y	Y	Y	Y	Y	Y	Y
Displacive	Y	Y	Y	Y	Y	N	Y	N	N

Table 3.5: Phase–transition characters of each component. 'Hardness–changing' includes bond softening and bond hardening, which are characterized by the change of the standard deviation of the Ti displacement distribution.

dergoes a change, even for the component(s) which is(are) non–polar before and after the transition. The transition(s) that each component undergoes are listed in Table 3.5.

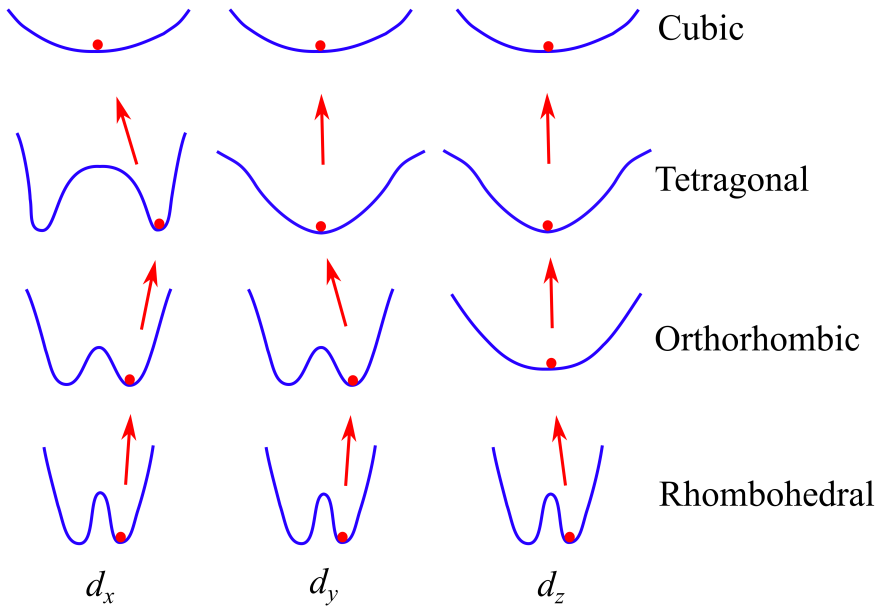

Figure 3.8: Schematic representations of bond–softening, bond–hardening and displacive excitations.).

In phenomenological models, people use order parameters, such as polarization or any modes, to describe the free energy [144, 145]. Geneste pointed out that free energy should be expressed with the density of probability (DOP) of the order parameter, rather than local order parameters [135]. DOP is defined as the average of the order parameters in a give region, and is characterized by its standard deviation. Our simulation is consistent with this

study, and all these results demonstrate that both the average and standard deviation of the polarization distribution are features of each specific phase.

3.6 Conclusion

In this work, we develop a classical atomistic potential for $BaTiO_3$ based on the bond valence model. Molecular dynamics simulation with this optimized potential can not only reproduce the temperature–driven phase transitions, but can also be a powerful tool in studying the phase transition process with high temporal and spatial resolutions. The detailed analysis of the local displacements of Ti atoms reveals that in each phase (including the paraelectric phase), the majority of Ti atoms are locally displaced, and the phase transitions in $BaTiO_3$ exhibit a mixture of order–disorder and displacive character. The distribution of Ti displacement is a Gaussian curve or a curve involving a Gaussian and a double peak one. By analyzing the dynamics of Ti displacement distributions during phase transition, we discover several rules of $BaTiO_3$ phase transitions: the global phase transition is associated with significant changes in each component, even for the components which are nonpolar, and the orthorhombic to tetragonal transition exhibits a bond–hardening character in the x component, which is opposite to the conventional understanding that temperature increase generally causes bond–softening transition.

Chapter 4

Giant negative unusual electrocaloric effect in ferroelectrics

4.1 Introduction

The electrocaloric effect (ECE) refers to the phenomenon in which the temperature of a material changes reversibly under the application and removal of electric field [146, 147, 148]. Recent years have seen a surge of interest in developing ECE–based cooling technology [149, 150, 151, 152, 153], which does not rely on the high global–warming potential refrigerants (hydrofluorocarbons and hydrochlorofluorocarbons) that are widely used in traditional vapor compression cooling technology. Giant positive ECEs up to 12 K have been observed in $PbZr_{0.95}Ti_{0.05}O_3$, and paving the path toward the practical application of the ECE is a fast–moving research project [154]. Similar to a mechanical refrigeration cycle, the traditional ECE–based refrigeration cycle involves four steps: (1) the temperature of a crystal increases under the application of electric field; (2) the crystal ejects heat to a sink; (3) the electric field is removed, and the temperature of the crystal decreases; (4) the crystal is contacted with a load and adsorbs heat from it [155]. It is generally assumed

the temperature decrease during the electric field removal should equal the temperature increase during the electric field application [156]. However, sometimes the cooling is less than expected, or even cannot be observed [152, 157, 158, 159]. The reasons include but are not limited to: the dielectric loss during the polarization relaxation, friction during the transfer of the crystal from the hot sink to the cold load, and entropy production during an irreversible process [157, 158, 159, 160]. Therefore, negative (anomalous) ECE, in which the temperature of a material will decrease (rather than increase) under an electric pulse, is significantly desired for effectively cooling the load [157, 161, 156].

In this work, we focus on a special kind of, unusual electrocaloric effect. It is denoted as 'unusual' because this temperature change is induced by just an electric field pulse and is an irreversible process. We demonstrate terahertz control of both positive and negative uECEs in ferroelectrics theoretically. We first clarify the mechanism of ECE from the energy conservation point of view, which can apply to both usual and unusual ECE. The external electric field does work on a ferrolectric crystal and causes structural change, which means a modification in potential energy. As a result, the kinetic energy, which relates to the temperature, also changes. The signs and magnitudes of these changes are determined by the electric field profile. Based on this improved understanding, we demonstrate that negative and giant uECE in prototypical ferroelectric $PbTiO_3$ can be realized with short electric field pulses, which correspond to giant cooling rates.

4.2 Theory

The ECE has been widely understood as entropy reallocation [147, 150, 156]. The application of electric field aligns dipoles in a material, and the configurational entropy is reduced. As a result, the thermal entropy, which corresponds to the lattice vibrations, increases. However, this mechanism only holds for a reversible adiabatic process, which

requires the system to be at equilibrium throughout. Ultra–fast uECE, which we will focus on in this study, is typically an irreversible process with non–zero entropy production, because the polarization does not have enough time to respond fully to the electric field. Besides, for a ferroelectric material system with thermal hysteresis, entropy production is also unavoidable in a loop. Because of the insufficiencies in explaining ECE in ferrolectrics with entropy reallocation, we propose that it is much more straightforward to understand the ECE with the concept of internal energy U (per unit volume) redistribution. Here, we should emphasize that from our MD simulation, the volume change is quite small (less than 1%). Therefore, the mechanical work is negligible, and the internal energy is very close to the enthalpy. The work W (per unit volume) done by electric field E is given as

$$W = \int \boldsymbol{E} \cdot \mathrm{d}\boldsymbol{P} \tag{4.1}$$

where $\boldsymbol{P}$ is the macroscopic polarization of the material at finite T. It is widely accepted that ECE occurs in a short time period, which allows little heat transfer [152, 156]. Therefore, the electrical work equals the internal energy change ΔU:

$$W = \Delta U = \Delta U_k + \Delta U_p \tag{4.2}$$

where ΔU_k and ΔU_p are changes in kinetic energy and potential energy. The temperature change ΔT is associated with ΔU_k as

$$\langle \Delta U_k \rangle = \frac{3}{2} k_B \Delta T N \implies \Delta T \propto \langle \Delta U_k \rangle \tag{4.3}$$

where N is the number of atoms per unit volume, k_B is the Boltzmann constant, and $\langle \Delta U_k \rangle$ denotes the ensemble average of the kinetic energy change ΔU_k. Generally, the direction of the polarization change $\mathrm{d}\boldsymbol{P}$ is along that of the applied electric field, and therefore W

is positive. In most cases, the applied electric field induces a more polar structure, which possesses lower potential energy for ferroelectric materials ($\Delta U_p < 0$). Therefore, ΔU_k is usually positive when turning on the electric field and negative when removing the electric field, causing heating and cooling respectively.

However, ΔU_k could be negative upon E field application, thus giving rise to negative ECE. For example, when there is a phase transition with positive transition energy $U_{\rm tr}$ (per unit volume), which is the difference of the potential energies of the two phases, induced by the applied electric field. $\Delta U_p \approx U_{\rm tr}$, and if $W < U_{\rm tr}$, we have $\Delta U_k = W - U_{\rm tr} < 0$. In this case, some kinetic energy goes to compensate the transition energy, and the temperature decreases.

Negative ECE is significant because it can offer a fast, direct and efficient cooling technique [161, 162, 156, 157, 163], where cooling is achieved through the application of electric field. It is one of the rare cases where doing work on a system causes its temperature to decrease. Here, we perform NPT (isobaric–isothermal) MD simulations with bond–valence–model based interatomic potentials, which have been proven reliable in simulating structural properties and dynamics of ferroelectrics under various conditions [115, 164, 122, 119, 165], to illustrate the theory of negative ECE in a realistic context. $10\times10\times10$ supercells (5000 atoms) were used for both $BaTiO_3$ and $PbTiO_3$. The temperature was controlled via the Nosé–Hoover thermostat [166, 167] and the pressure was maintained at 1 atm via the Parrinello–Rahman barostat [132]. Each simulation was performed with a 0.5 fs time step. For simulating equilibrium states, the thermal inertia M_s was selected as 1.0 amu, in order to control the temperature effectively [166, 167]. Adiabatic MD simulations for the pulse application or removal period began with equilibrated states, and M_s was set with an extremely large value (50000), in order to prohibit heat transfer [156]. Therefore, these simulations are adiabatic, aiming to describe the structural and temperature change during the short pulse period, rather than isobaric–isothermal

long–trajectory simulations, which describe the equilibrium states at a specific temperature and pressure. The parameters of the bond valence model, the method of calculating local polarization, and the phase transition temperatures given by this model are described in references [119, 163]. It is also worth mentioning that the transition temperatures are usually underestimated in our bond–valence model. However, this would not greatly affect the applicability of this potential [115, 164, 122, 119, 165], and the mechanisms of such underestimations are given in references [119, 163]. For practical application, these temperatures could be scaled.

4.3 Results

At 101 K, a $BaTiO_3$ crystal is in its rhombohedral phase in our MD simulations. An 80 kV/cm electric field along the (110) direction is applied to drive the system from the rhombohedral to the orthorhombic phase. As shown in Fig. 4.1 (a), the polarization components along the x and y directions (P_x and P_y, parallel to E) increase a bit ($\Delta P_i = 0.04$ C/m^2), indicating that the work W done by the electric field E is small. The crystal is driven to the orthorhombic phase, accompanied by an increase of the potential energy, because there is a transition energy $U_{\rm tr}$ for the rhombohedral to orthorhombic phase transition, as shown in Fig. 4.1 (a) and (b). Since

$$W \approx 0,\ \Delta U_p = U_{\rm tr} > 0, \tag{4.4}$$

$$\Delta U_k = W - \Delta U_p < 0, \tag{4.5}$$

we observe in MD simulations a decrease in temperature, with an ultra–fast cooling rate ($\approx 10^{11}$ K/s). Based on the equation (4.5), which demonstrates that negative ECE requires

W to be smaller than $U_{\rm tr}$, we can estimate the upper limit of electric field $E_{\rm max}$ causing temperature decrease in our BTO MD model:

$$W - \Delta U_p < 0,\ \boldsymbol{E_{\rm max}}\cdot\Delta\boldsymbol{P} < U_{\rm tr} \tag{4.6}$$

$$E_{{\rm max},i} < \frac{U_{\rm tr}}{\Delta P_i} \approx 800\ {\rm kV/cm}. \tag{4.7}$$

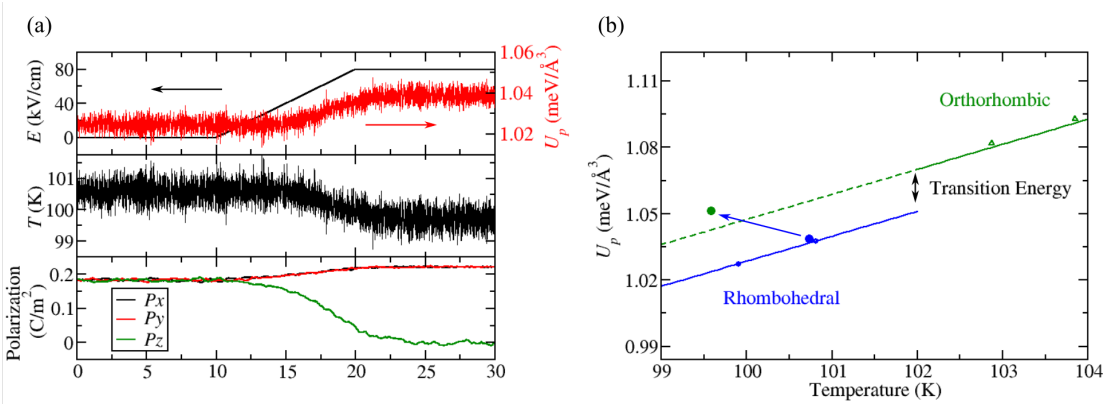

Figure 4.1: Negative electrocaloric effect associated with the rhombohedral to orthorhombic phase transition in $BaTiO_3$. (a) Electric field, potential energy, temperature and polarization *vs.* time. (b) Schematic plot of potential energy *vs.* temperature for the two phases, demonstrating the electric field–induced phase transition and ultra–fast temperature reduction.

Similarly, we can also generate a negative ECE through the orthorhombic to tetragonal phase transition. The case for tetragonal to cubic phase transition is less straightforward, because no unidirectional quasi–static electric field can induce the tetragonal to cubic phase transition. Simulations demonstrate that the cubic phase of $BaTiO_3$ crystal has a disorder character [137, 141, 142]; the dipoles in various unit cells orient in different directions and vary with time, and the macroscopic polarization is zero [163]. Here, we design a single cycle terahertz pulse [168, 120] which is perpendicular to the tetragonal phase polarization. A rapidly oscillating electric field pulse can disorder the polarization, effectively changing

the system to the cubic phase. The post–pulse state behaves as a supercooled cubic phase. We highlight that pulse–induced negative uECE requires the occurrence of a phase transition. In the absence of field–driven phase transition, because of the one–to–one relationship between energy and temperature in the same phase, the system with higher energy will have higher temperature. The temperature decrease due to tetragonal–cubic transition in BTO is larger ($\approx$ 2 K) than that due to orthorhombic–tetragonal transition, as shown in Fig. 4.2 (a), which is directly related to the larger transition energy of the tetragonal–cubic phase transition.

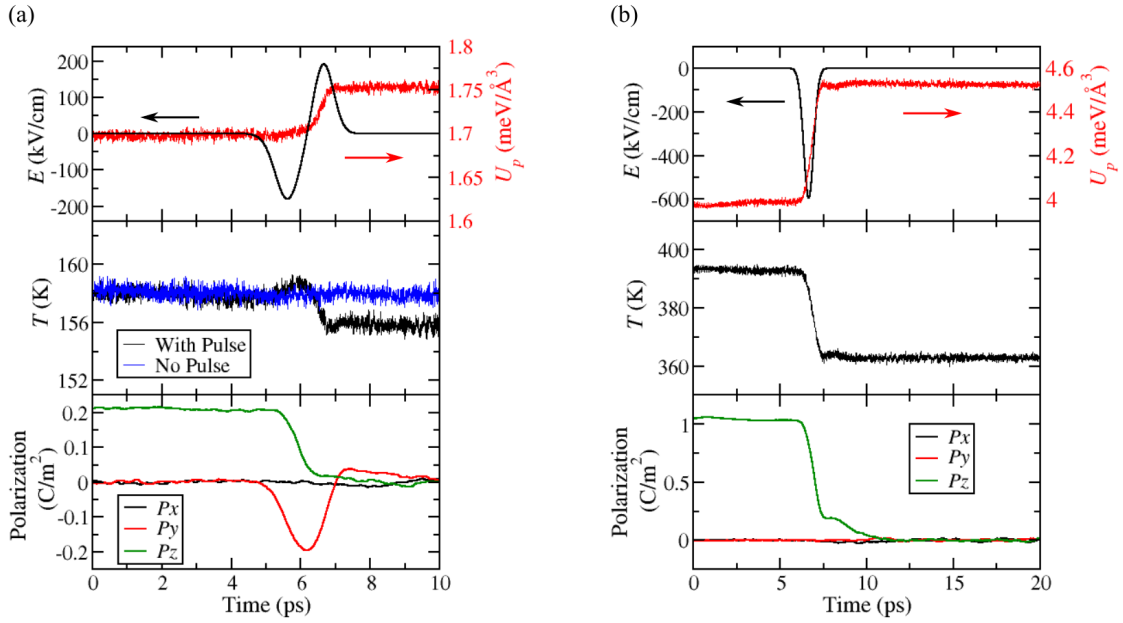

Figure 4.2: Time evolution of the electric–field pulse, potential energy, temperature, and polarization along the three Cartesian axes for (a) $BaTiO_3$, under a single–cycle THz electric field pulse perpendicular to the polarization in tetragonal $BaTiO_3$. (b) $PbTiO_3$, under a half–cycle THz electric field pulse anti–parallel to polarization in $PbTiO_3$.

From the analysis above, we demonstrate that negative uECE can be achieved with E–field–induced phase transitions from the low–temperature phase to the high–temperature phase, because some of the kinetic energy is lost to compensate the potential energy increase. Conversely, if the transition is from high–temperature phase to low, temperature

increases and we find positive ECE. In Fig. 4.3, we plot the temperature changes of $BaTiO_3$ and $PbTiO_3$, under the application of a 600 kV/cm electric field. We observe $\Delta T = 9.0$ K, 50.0 K respectively for $BaTiO_3$ and $PbTiO_3$. The temperature change (for the same electric field) for $PbTiO_3$ is giant and about five times of that for $BaTiO_3$. This is attributed to its larger transition energy (five times that of $BaTiO_3$).

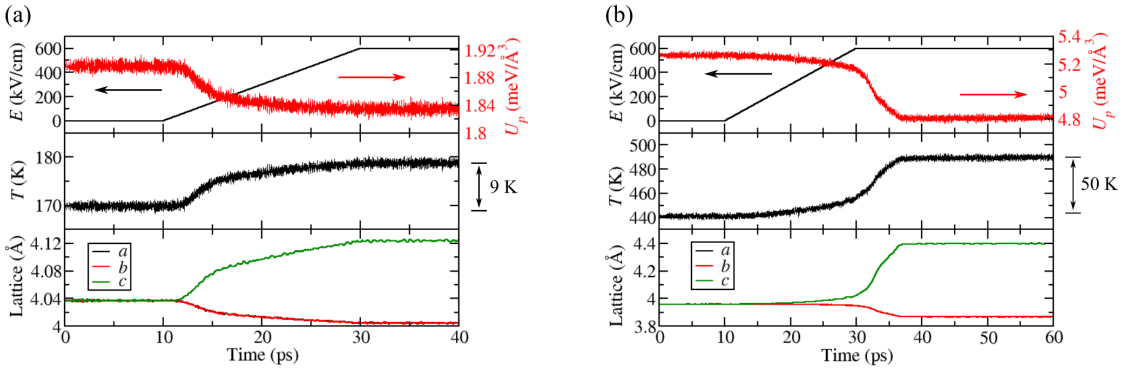

Figure 4.3: Time evolution of the electric–field pulse, potential energy, temperature, and lattice constants for $BaTiO_3$ and $PbTiO_3$ under the application of a 600 kV/cm electric field.

We also predict large negative uECE in $PbTiO_3$. An ultra–fast electric–field pulse is applied anti–parallel to the $PbTiO_3$ polarization, as shown in Fig. 4.2 (b). This electric–field pulse induces some negative local polarization in a positively polarized crystal. This does work $W = \int \boldsymbol{E} \cdot \mathrm{d}\boldsymbol{P} > 0$. The polarization evolution in the Gibbs free energy profile is shown in Fig. 4.4. After the pulse, the system passes the energy barrier between the tetragonal and cubic phases, and the system evolves to a local minimum corresponding to cubic phase without any external force. As expected, this E pulse induces a tetragonal–to–cubic phase transition, and a 32 K temperature decrease is observed, which is much higher than recent experimental observation [169, 170, 171, 172, 173]. This supercooled cubic phase crystal can be used in a cooling cycle. After adsorbing heat and equilibrating with a load, the crystal is contacted with a sink. Application of a quasi–static electric field can drive it back to its original phase with a higher temperature, and then the crystal gives off

heat and cools to its original state.

These results indicate that a large transition energy is critical for giant uECE. The transition energy sets the upper limit for negative ECE, according to equations (4.3) and (4.5):

$$\Delta T_{\max} = \frac{2U_{\mathrm{tr}}}{3k_B N}. \tag{4.8}$$

Gibbs free energy, which takes entropy into consideration, reveals the stability of a specific phase at a certain temperature [174, 175]. It should be emphasized that a triple well Gibbs free energy landscape, as shown in Fig. 4.4, is necessary for such an E–pulse–induced negative uECE. This requires temperature close to the Curie temperature T_C. Around T_C, the free energies of the polar and non–polar states are so close that the driving force for polar domain wall nucleation and growth is very low. As a result, the applied E pulse tends to disrupt the local polarization and trigger the phase transition, rather than induce domains. Our simulations demonstrate that the metastable cubic phase of $PbTiO_3$ can last for a long time period (more than 20 ns), which is long enough for heat transfer. This is because the transition from a metastable cubic structure to a tetragonal one begins with the nucleation of a small region with local parallel polarization. However, this appearance of the polar nuclei costs domain wall energy, which is unfavorable around T_C [176, 165], as demonstrated in Fig. 4.4. In summary, we desire two phases with a large difference in potential energy, in order to acquire large temperature change, and a small difference in Gibbs free energy, so that the metastable high–temperature phase lasts a long time and can be induced by an electric field pulse.

Though $PbTiO_3$ exhibits a giant uECE effect near T_c, its high T_c (765 K in experiments) may impede practical applications at room temperature [177]. Techniques that can suppress T_c of $PbTiO_3$–based ferroelectrics such as doping and strain engineering will be helpful for developing practical negative ECE materials [178]. Another practical concern is that Joule

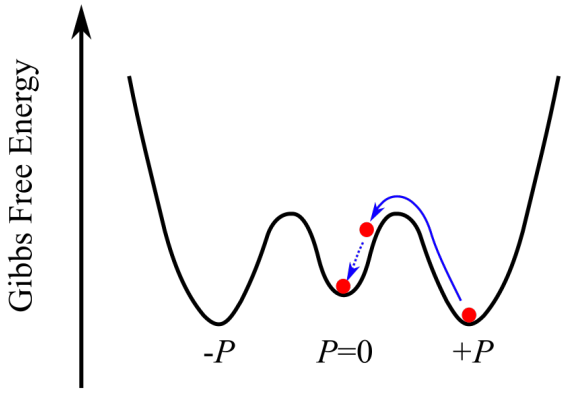

Figure 4.4: Schematic representation of the polarization evolution in the Gibbs free energy profile. The outer two minima represent the states with positive and negative polarization. The central minimum represents a cubic phase.

heating may counteract negative ECE. Joule heating depends on the conductivity of the sample and the field duration, and the conductivity of prototypical ferroelectrics could be affected significantly by soft–mode absorption at THz frequencies. A previous combined theoretical and experimental study demonstrates that for $BaTiO_3$ at THz frequencies, the dielectric loss calculated from first–principles based MD matches that acquired from experimental measurement [179], indicating that the soft–mode related conductivity of $BaTiO_3$ is included appropriately in MD simulations. Moreover, previous experiments also suggest that $PbTiO_3$, which we predict to show giant pulse–induced negative ECE in this study, has low conductivity (and heating) under THz excitation. [180].

4.4 Conclusion

In this study, we analyze and explain ECE from an energy point of view: the electric field does work on a crystal, reallocates its kinetic and potential energies, and causes temperature change. We propose that negative uECE can be both ultra–fast and giant (T reduction as high as 32 K), and a low–temperature to high–temperature phase transition is required in such an E–pulse–induced uECE. The cooling rate due to pulse-induced negative uECE is

fast ($\approx 10^{11}$ K/s), because of the fast response of polarization in prototypical ferroelectrics to electric field (in picoseconds).

Bibliography

[1] Miller, S.; McWhorter, P. *Journal of applied physics* **1992**, *72*, 5999–6010.

[2] Mathews, S.; Ramesh, R.; Venkatesan, T.; Benedetto, J. *Science* **1997**, *276*, 238–240.

[3] Ma, T.; Han, J.-P. *Electron Device Letters, IEEE* **2002**, *23*, 386–388.

[4] Spanier, J. E.; Kolpak, A. M.; Urban, J. J.; Grinberg, I.; Ouyang, L.; Yun, W. S.; Rappe, A. M.; Park, H. *Nano Lett.* **2006**, *6*, 735–9.

[5] Urban, J. J.; Yun, W. S.; Gu, Q.; Park, H. *Journal of the American Chemical Society* **2002**, *124*, 1186–1187.

[6] Yun, W. S.; Urban, J. J.; Gu, Q.; Park, H. *Nano Lett.* **2002**, *2*, 447–450.

[7] Urban, J.; Spanier, J.; Ouyang, L.; Yun, W.; Park, H. *Adv. Mater.* **2003**, *15*, 423–426.

[8] Batra, I. P.; Silverman, B. D. *Solid State Commun.* **1972**, *11*, 291–4.

[9] Nonnenmann, S. S.; Spanier, J. E. *Journal of materials science* **2009**, *44*, 5205–5213.

[10] Stengel, M.; Spaldin, N. *Nature* **2006**, *443*, 679–682.

[11] Szwarcman, D.; Lubk, A.; Linck, M.; Vogel, K.; Lereah, Y.; Lichte, H.; Markovich, G. *Physical Review B* **2012**, *85*, 134112.

[12] Szwarcman, D.; Prosandeev, S.; Louis, L.; Berger, S.; Rosenberg, Y.; Lereah, Y.; Bellaiche, L.; Markovich, G. *Journal of Physics: Condensed Matter* **2014**, *26*, 122202.

[13] Kim, D.; Jo, J.; Kim, Y.; Chang, Y.; Lee, J.; Yoon, J.-G.; Song, T.; Noh, T. *Physical review letters* **2005**, *95*, 237602.

[14] Saidi, W. A.; Martirez, J. M. P.; Rappe, A. M. *Nano Lett.* **2014**, *14*, 6711–6717.

[15] Kolpak, A. M.; Li, D.; Shao, R.; Rappe, A. M.; Bonnell, D. A. *Phys. Rev. Lett.* **2008**, *101*, 036102–1–4.

[16] Mendez-Polanco, M. A.; Grinberg, I.; Kolpak, A. M.; Levchenko, S. V.; Pynn, C.; Rappe, A. M. *Phys. Rev. B* **2012**, *85*, 214107.

[17] Sai, N.; Kolpak, A. M.; Rappe, A. M. *Phys. Rev. B Rapid Comm.* **2005**, *72*, 020101(R)–1–4.

[18] Kolpak, A. M.; Sai, N.; Rappe, A. M. *Phys. Rev. B* **2006**, *74*, 054112–1–5.

[19] Stengel, M.; Vanderbilt, D.; Spaldin, N. *Nat. Mater.* **2009**, *8*, 392–397.

[20] Fong, D. D.; Kolpak, A. M.; Eastman, J. A.; Streiffer, S. K.; Fuoss, P. H.; Stephenson, G. B.; Thompson, C.; Kim, D. M.; Choi, K. J.; Eom, C. B.; Grinberg, I.; Rappe, A. M. *Phys. Rev. Lett.* **2006**, *96*, 127601.

[21] Li, D.; Zhao, M. H.; Garra, J.; Kolpak, A.; Rappe, A.; Bonnell, D. A.; Vohs, J. M. *Nature Mater.* **2008**, *7*, 473–7.

[22] Wang, R. V.; Fong, D. D.; Jiang, F.; Highland, M. J.; Fuoss, P. H.; Thompson, C.; Kolpak, A. M.; Eastman, J. A.; Streiffer, S. K.; Rappe, A. M.; Stephenson, G. B. *Phys. Rev. Lett.*. **2009**, *102*, 047601 1–4.

[23] Koocher, N. Z.; Martirez, J. M. P.; Rappe, A. M. *J. Phys. Chem. Lett.* **2014**, *5*, 3408–3414.

[24] Stephenson, G. B.; Highland, M. J. *Physical Review B* **2011**, *84*, 064107.

[25] Levchenko, S. V.; Rappe, A. M. *Phys. Rev. Lett.* **2008**, *100*, 256101.

[26] He, D.; Qiao, L.; Volinsky, A. A.; Bai, Y.; Wu, M.; Chu, W. *Applied Physics Letters* **2011**, *98*, 062905–062905.

[27] He, D.; Qiao, L.; Volinsky, A. A.; Bai, Y.; Guo, L. *Physical Review B* **2011**, *84*, 024101.

[28] Kalinin, S. V.; Johnson, C. Y.; Bonnell, D. A. *J. Appl. Phys.* **2002**, *91*, 3816–23.

[29] Noma, T.; Wada, S.; Yano, M.; Suzuki, T. *J. Appl. Phys.* **1996**, *80*, 5223–33.

[30] Wegmann, M.; Watson, L.; Hendry, A. *Journal of the American Ceramic Society* **2004**, *87*, 371–377.

[31] Giannozzi, P.; Baroni, S.; Bonini, N.; Calandra, M.; et al. *J. Phys.: Condens. Matter* **2009**, *21*, 395502–20.

[32] Al-Saidi, W. A.; Rappe, A. M. *Phys. Rev. B* **2010**, *82*, 155304.

[33] http://opium.sourceforge.net.

[34] Monkhorst, H. J.; Pack, J. D. *Phys. Rev. B* **1976**, *13*, 5188–5192.

[35] Burstein, E.; Lundqvist, S. *Tunneling phenomena in solids*; Plenum Press: New York, 1969.

[36] Dekker, A. *Solid State Physics*; Prentice–Hall, INC.: Englewood Cliffs, N. J., 1957.

[37] Simmons, J. *Physical Review Letters* **1965**, *15*, 967.

[38] Pyykko, P.; Laaksonen, L. *The Journal of Physical Chemistry* **1984**, *88*, 4892–4895.

[39] Rappe, A. M.; Rabe, K. M.; Kaxiras, E.; Joannopoulos, J. D. *Phys. Rev. B Rapid Comm.* **1990**, *41*, 1227–30.

[40] McQuarrie, D. D. A.; Simon, J. J. D. *Physical chemistry: a molecular approach*; University Science Books, 1997.

[41] Zafar, S.; Jones, R. E.; Jiang, B.; White, B.; Kaushik, V.; Gillespie, S. *Applied physics letters* **1998**, *73*, 3533–3535.

[42] Ziman, J. *Electronics and Phonons*; Clarendon Press, Oxford: London, 1960.

[43] Low, F. E.; Pines, D. *Physical Review* **1955**, *98*, 414.

[44] Schultz, T. *Physical Review* **1959**, *116*, 526.

[45] Wemple, S.; DiDomenico Jr, M.; Jayaraman, A. *Physical Review* **1969**, *180*, 547.

[46] Spigler, R.; Vianello, M. *Advances in Difference Equations (Veszprém, 1995)* **1995**, 567–577.

[47] Lyddane, R. H.; Sachs, R.; Teller, E. *Phys. Rev.* **1941**, *59*, 673–6.

[48] Shirane, G.; Frazer, B.; Minkiewicz, V.; Leake, J.; Linz, A. *Physical Review Letters* **1967**, *19*, 234.

[49] Rabe, K. M.; Ahn, C. H.; Triscone, J.-M. *Physics of Ferroelectrics: A Modern Perspective*; Springer-Verlag, 2007.

[50] Singh, D. J. *Phys. Rev. B* **1996**, *53*, 176–80.

[51] Benedict, T.; Durand, J. *Physical Review* **1958**, *109*, 1091.

[52] Barker Jr, A. *Physical Review* **1966**, *145*, 391.

[53] Wurfel, P.; Batra, I. P. *Phys. Rev. B* **1973**, *8*, 5126–39.

[54] Mehta, R. R.; Silverman, B. D.; Jacobs, J. T. *J. Appl. Phys.* **1973**, *44*, 3379–85.

[55] Berglund, C.; Baer, W. *Physical Review* **1967**, *157*, 358.

[56] Boyeaux, J.; Michel-Calendini, F. *Journal of Physics C: Solid State Physics* **1979**, *12*, 545.

[57] Fridkin, V.; Grekov, A.; Rodin, A.; Savchenko, E.; Volk, T. *Ferroelectrics* **1973**, *6*, 71–82.

[58] Vinetskii, V.; Itskovskii, M.; Kukushkin, L. *physica status solidi (b)* **1970**, *39*, K23–K27.

[59] Burgess, R. E.; Weiss, G. *Physics Today* **1965**, *18*, 60.

[60] Shockley, W. *Electrons and holes in semiconductors*; D. Van Nostrand Company, Inc.: New York, 1950.

[61] Kittel, C.; McEuen, P. *Introduction to solid state physics*; Wiley New York, 1986; Vol. 8.

[62] Cardona, M. *Physical Review* **1965**, *140*, A651–&.

[63] Dietz, G.; Schumacher, M.; Waser, R.; Streiffer, S.; Basceri, C.; Kingon, A. *Journal of applied physics* **1997**, *82*, 2359.

[64] Gruverman, A.; Wu, D.; Lu, H.; Wang, Y.; Jang, H.; Folkman, C.; Zhuravlev, M. Y.; Felker, D.; Rzchowski, M.; Eom, C.-B.; et al. *Nano Lett.* **2009**, *9*, 3539–3543.

[65] Garcia, V.; Fusil, S.; Bouzehouane, K.; Enouz-Vedrenne, S.; Mathur, N. D.; Barthelemy, A.; Bibes, M. *Nature* **2009**, *460*, 81–84.

[66] Chen, J.; Chan, T.; Chen, I.; Ko, P.; Hu, C. *IEEE Electron Device Lett.* **1987**, *8*, 515–517.

[67] Taur, Y.; Ning, T. H.; et al. *Fundamentals of modern VLSI devices*; Cambridge University Press Cambridge, 1998; Vol. 2.

[68] Salahuddin, S.; Datta, S. *Nano letters* **2008**, *8*, 405–410.

[69] Loh, O. Y.; Espinosa, H. D. *Nature Nanotechnol.* **2012**, *7*, 283–295.

[70] Spencer, M.; Chen, F.; Wang, C. C.; Nathanael, R.; Fariborzi, H.; Gupta, A.; Kam, H.; Pott, V.; Jeon, J.; Liu, T.-J. K.; Markovic, D.; Alon, E.; Stojanovic, V. *IEEE J. Solid–State Circuits* **2011**, *46*, 308–320.

[71] Lee, J. O.; Song, Y.-H.; Kim, M.-W.; Kang, M.-H.; Oh, J.-S.; Yang, H.-H.; Yoon, J.-B. *Nature Nanotechnol.* **2013**, *8*, 36–40.

[72] Sinha, N.; Jones, T. S.; Guo, Z.; Piazza, G. *J. Microelectromech. Syst.* **2012**, *21*, 484–496.

[73] Czaplewski, D. A.; Patrizi, G. A.; Kraus, G. M.; Wendt, J. R.; Nordquist, C. D.; Wolfley, S. L.; Baker, M. S.; De Boer, M. P. *Journal of Micromechanics and Microengineering* **2009**, *19*, 085003.

[74] Dickrell, D.; Dugger, M. T. *IEEE Trans. Compon. Packag. Technol.* **2007**, *30*, 75–80.

[75] Jensen, B. D.; Chow, L. L.-W.; Huang, K.; Saitou, K.; Volakis, J. L.; Kurabayashi, K. *J. Microelectromech. Syst.* **2005**, *14*, 935–946.

[76] Brand, V.; Baker, M. S.; de Boer, M. P. *Tribol. Lett.* **2013**, *51*, 341–356.

[77] Brand, V.; Baker, M. S.; de Boer, M. P. *J. Microelectromech. Syst.* **2013**, *22*, 1248–1250.

[78] Hermance, H.; Egan, T. *Bell Syst. Tech. J.* **1958**, *37*, 739–776.

[79] van Spengen, W. M. *Microelectronics Reliability* **2003**, *43*, 1049–1060.

[80] Hyman, D.; Mehregany, M. *IEEE Trans. Compon. and Pack. Tech.* **1999**, *22*, 357–364.

[81] Patton, S.; Zabinski, J. *Tribol. Lett.* **2005**, *18*, 215–230.

[82] Yang, Z.; Lichtenwalner, D. J.; Morris, A. S.; Krim, J.; Kingon, A. I. *J. Microelectromech. Syst.* **2009**, *18*, 287–295.

[83] Tringe, J. W.; Uhlman, T. A.; Oliver, A. C.; Houston, J. E. *J. Appl. Phys.* **2003**, *93*, 4661–4669.

[84] Wabiszewski, G. E. *Diploma Thesis* **2013**, 1–156.

[85] Saeys, M.; Reyniers, M.-F.; Marin, G. B.; Neurock, M. *J. Phys. Chem. B* **2002**, *106*, 7489–7498.

[86] Walter, E. J.; Rappe, A. M. *Surf. Sci.* **2004**, *549*, 265–72.

[87] Watson, G. W.; Wells, R. P.; Willock, D. J.; Hutchings, G. J. *J. Phys. Chem. B* **2001**, *105*, 4889–4894.

[88] Henkelman, G.; Uberuaga, B. P.; Jónsson, H. *J. Chem. Phys.* **2000**, *113*, 9901–4.

[89] Black, A. L.; Lenhardt, J. M.; Craig, S. L. *J. Mater. Chem.* **2011**, *21*, 1655–1663.

[90] Bell, G. I. *Science* **1978**, *200*, 618–627.

[91] Konda, S. S. M.; Brantley, J. N.; Bielawski, C. W.; Makarov, D. E. *J Chem. Phys.* **2011**, *135*, 164103.

[92] Saeys, M.; Reyniers, M.-F.; Neurock, M.; Marin, G. B. *J. Phys. Chem. B* **2003**, *107*, 3844–3855.

[93] Trevor, D. J.; Whetten, R. L.; Cox, D. M.; Kaldor, A. *J. Am. Chem. Soc.* **1985**, *107*, 518–519.

[94] Tsai, M. C.; Friend, C. M.; Muetterties, E. L. *J. Am. Chem. Soc.* **1982**, *104*, 2539–2543.

[95] Martirez, J. M. P.; Kim, S.; Morales, E. H.; Diroll, B. T.; Cargnello, M.; Gordon, T. R.; Murray, C. B.; Bonnell, D. A.; Rappe, A. M. *J. Am. Chem. Soc.* **2015**, *137*, 2939–2947.

[96] Hammer, B.; Norskov, J. *Nature* **1995**, *376*, 238–240.

[97] Wen, X.-D.; Hoffmann, R.; Ashcroft, N. *J. Am. Chem. Soc.* **2011**, *133*, 9023–9035.

[98] Chen, K.-H.; Chen, Y.-C.; Chen, Z.-S.; Yang, C.-F.; Chang, T.-C. *Appl. Phys. A Mater. Sci.* **2007**, *89*, 533–536.

[99] Buessem, W.; Cross, L.; Goswami, A. *J. Am. Ceram. Soc.* **1966**, *49*, 33–36.

[100] Karaki, T.; Yan, K.; Adachi, M. *Jpn. J. of Appl. Phys.* **2007**, *46*, 7035.

[101] Cohen, R. E. *Ferroelectrics* **1992**, *136*, 65–83.

[102] Gonze, X.; Lee, C. *Phys. Rev. B* **1997**, *55*, 10355–68.

[103] Saha, S.; Sinha, T.; Mookerjee, A. *Phys. Rev. B* **2000**, *62*, 8828.

[104] Martirez, J. M. P.; Morales, E. H.; Al-Saidi, W. A.; Bonnell, D. A.; Rappe, A. M. *Phys. Rev. Lett.* **2012**, *109*, 256802 1–5.

[105] Morales, E. H.; Martirez, J. M. P.; Saidi, W. A.; Rappe, A. M.; Bonnell, D. A. *ACS nano* **2014**, *8*, 4465–4473.

[106] Zhong, W.; Vanderbilt, D.; Rabe, K. M. *Phys. Rev. Lett.* **1994**, *73*, 1861–4.

[107] Zhong, W.; Vanderbilt, D.; Rabe, K. M. *Phys. Rev. B* **1995**, *52*, 6301–12.

[108] Nishimatsu, T.; Waghmare, U. V.; Kawazoe, Y.; Vanderbilt, D. *Phys. Rev. B* **2008**, *78*, 104104.

[109] Fu, H.; Bellaiche, L. *Phys. Rev. Lett.* **2003**, *91*, 257601–1–4.

[110] Tinte, S.; Stachiotti, M. G.; Sepliarsky, M.; Migoni, R. L.; Rodriquez, C. O. *J. Phys.: Condens. Matter* **1999**, *11*, 9679–90.

[111] Tinte, S.; Stachiotti, M. G. *Phys. Rev. B* **2001**, *64*, 235403–1–7.

[112] Tinte, S.; Stachiotti, M.; Sepliarsky, M.; Migoni, R.; Rodriguez, C. *Ferroelectrics* **2000**, *237*, 41–48.

[113] Zhang, Y.; Hong, J.; Liu, B.; Fang, D. *Nanotechnology* **2010**, *21*, 015701.

[114] Zhang, Y.; Hong, J.; Liu, B.; Fang, D. *Nanotechnology* **2009**, *20*, 405703.

[115] Grinberg, I.; Cooper, V. R.; Rappe, A. M. *Nature* **2002**, *419*, 909–911.

[116] Shin, Y.-H.; Son, J.-Y.; Lee, B.-J.; Grinberg, I.; Rappe, A. M. *J. Phys.: Condens. Matter* **2008**, *20*, 015224–1–5.

[117] Shin, Y.-H.; Cooper, V. R.; Grinberg, I.; Rappe, A. M. *Phys. Rev. B* **2005**, *71*, 054104–1–4.

[118] Liu, S.; Grinberg, I.; Rappe, A. M. *J. Physics.: Condens. Matter* **2013**, *25*, 102202 1–6.

[119] Liu, S.; Grinberg, I.; Takenaka, H.; Rappe, A. M. *Phys. Rev. B* **2013**, *88*, 104102 1–7.

[120] Chen, F.; Goodfellow, J.; Liu, S.; Grinberg, I.; Hoffmann, M. C.; Damodaran, A. R.; Zhu, Y.; Zalden, P.; Zhang, X.; Takeuchi, I.; et al. *Adv. Mater.* **2015**, *27*, 6371–6375.

[121] Liu, S.; Grinberg, I.; Rappe, A. M. *Appl. Phys. Lett.* **2013**, *103*, 232907 1–4.

[122] Xu, R.; Liu, S.; Grinberg, I.; Karthik, J.; Damodaran, A. R.; Rappe, A. M.; Martin, L. W. *Nat. Mater.* **2015**, *14*, 79–86.

[123] Kwei, G.; Lawson, A.; Billinge, S.; Cheong, S. *J. Phys. Chem.* **1993**, *97*, 2368–2377.

[124] Diéguez, O.; Tinte, S.; Antons, A.; Bungaro, C.; Neaton, J. B.; Rabe, K. M.; Vanderbilt, D. *Phys. Rev. B* **2004**, *69*, 212101 1–4.

[125] Von Hippel, A. *Rev. Mod. Phys.* **1950**, *22*, 221.

[126] Brown, I. D. *Chem. Rev.* **2009**, *109*, 6858–6919.

[127] Brown, I.; Shannon, R. *Acta Cryst.* **1973**, *A 29*, 266–82.

[128] Brown, I.; Wu, K. K. *Acta. Cryst.* **1976**, *B32*, 1957–9.

[129] Finnis, M.; Sinclair, J. *Philos. Mag. A* **1984**, *50*, 45–55.

[130] Harvey, M. A.; Baggio, S.; Baggio, R. *Acta Crystallogr. B* **2006**, *62*, 1038–1042.

[131] Perdew, J.; Ruzsinszky, A.; Gábor, C.; Vydrov, O.; Scuseria, G.; Constantin, L.; Zhou, X.; Burke, K. *Phys. Rev. Lett.* **2008**, *100*, 136406–1 – 4.

[132] Parrinello, M.; Rahman, A. *Phys. Rev. Lett.* **1980**, *45*, 1196.

[133] Ghosez, P.; Gonze, X.; Lambin, P.; Michenaud, J.-P. *Phys. Rev. B* **1995**, *51*, 6765.

[134] Vielma, J. M.; Schneider, G. *J. Appl. Phys.* **2013**, *114*, 174108.

[135] Geneste, G. *J. Phys. Condens. Matter* **2011**, *23*, 125901.

[136] Cohen, R. E.; Krakauer, H. *Phys. Rev. B* **1990**, *42*, 6416–23.

[137] Gaudon, M. *Polyhedron* **2015**, *88*, 6–10.

[138] Ehses, K.; Bock, H.; Fischer, K. *Ferroelectrics* **1981**, *37*, 507–510.

[139] Jun, C.; Chan-Gao, F.; Qi, L.; Duan, F. *J Phys. C: Solid State Phys.* **1988**, *21*, 2255.

[140] Comes, R.; Lambert, M.; Guinier, A. *Solid State Commun.* **1968**, *6*, 715–719.

[141] Itoh, K.; Zeng, L.; Nakamura, E.; Mishima, N. *Ferroelectrics* **1985**, *63*, 29–37.

[142] Stern, E. A. *Phys. Rev. Lett.* **2004**, *93*, 037601.

[143] Gaffney, K. J.; Chapman, H. N. *Science* **2007**, *316*, 1444–1448.

[144] Pertsev, N. A.; Zembilgotov, A. G.; Tagantsev, A. K. *Phys. Rev. Lett.* **1998**, *80*, 1988–91.

[145] Koukhar, V. G.; Pertsev, N. A.; Waser, R. *Phys. Rev. B* **2001**, *64*, 214103–1–15.

[146] Rose, M. C.; Cohen, R. E. *Phys. Rev. Lett.* **2012**, *109*, 187604.

[147] Takeuchi, I.; Sandeman, K. *Phys. Today* **2015**, *68*, 48–53.

[148] Moya, X.; Kar-Narayan, S.; Mathur, N. D. *Nat. Mater.* **2014**, *13*, 439–450.

[149] Lu, S.-G.; Zhang, Q. *Adv. Mater.* **2009**, *21*, 1983–1987.

[150] Valant, M. *Prog. Mater Sci.* **2012**, *57*, 980–1009.

[151] Manosa, L.; Planes, A.; Acet, M. *J. Mater. Chem. A* **2013**, *1*, 4925–4936.

[152] Scott, J. F. *Annu. Rev. Mater. Res.* **2011**, *41*, 229–240.

[153] Neese, B.; Chu, B.; Lu, S.-G.; Wang, Y.; Furman, E.; Zhang, Q. M. *Science* **2008**, *321*, 821–823.

[154] Mischenko, A. S.; Zhang, Q.; Scott, J. F.; Whatmore, R. W.; Mathur, N. D. *Science* **2006**, *311*, 1270–1271.

[155] Akcay, G.; Alpay, S. P.; Mantese, J. V.; Rossetti, G. A. *Appl. Phys. Lett.* **2007**, *90*, 2909.

[156] Ponomareva, I.; Lisenkov, S. *Phys. Rev. Lett.* **2012**, *108*, 167604.

[157] Qian, X.; Yang, T.; Zhang, T.; Chen, L.-Q.; Zhang, Q. M. *Appl. Phys. Lett.* **2016**, *108*, 142902.

[158] Gu, H.; Qian, X.; Li, X.; Craven, B.; Zhu, W.; Cheng, A.; Yao, S. C.; Zhang, Q. M. *Appl. Phys. Lett.* **2013**, *102*, 122904.

[159] Plaznik, U.; Kitanovski, A.; Rožič, B.; Malič, B.; Uršič, H.; Drnovšek, S.; Cilenšek, J.; Vrabelj, M.; Poredoš, A.; Kutnjak, Z. *Appl. Phys. Lett.* **2015**, *106*, 043903.

[160] Plaznik, U.; Vrabelj, M.; Kutnjak, Z.; Malič, B.; Poredoš, A.; Kitanovski, A. *Europhys. Lett.* **2015**, *111*, 57009.

[161] Pirc, R.; Rožič, B.; Koruza, J.; Malič, B.; Kutnjak, Z. *EPL* **2014**, *107*, 17002.

[162] Geng, W.; Liu, Y.; Meng, X.; Bellaiche, L.; Scott, J. F.; Dkhil, B.; Jiang, A. *Adv. Mater.* **2015**, *27*, 3165–3169.

[163] Qi, Y.; Liu, S.; Grinberg, I.; Rappe, A. M. *Phys. Rev. B* **2016**, *94*, 134308.

[164] Shin, Y.-H.; Grinberg, I.; Chen, I.-W.; Rappe, A. M. *Nature* **2007**, *449*, 881–6.

[165] Liu, S.; Grinberg, I.; Rappe, A. M. *Nature* **2016**, *534*, 360–363.

[166] Hoover, W. G. *Phys. Rev. A* **1985**, *31*, 1695–7.

[167] Nosé, S. *J. Chem. Phys.* **1984**, *81*, 511–9.

[168] Qi, T.; Shin, Y. H.; Yeh, K. L.; Nelson, K. A.; Rappe, A. M. *Phys. Rev. Lett.* **2009**, *102*, 247603 1–4.

[169] Guyomar, D.; Sebald, G.; Guiffard, B.; Seveyrat, L. *J. Phys. D: Appl. Phys.* **2006**, *39*, 4491.

[170] Sebald, G.; Pruvost, S.; Seveyrat, L.; Lebrun, L.; Guyomar, D.; Guiffard, B. *J. Eur. Ceram. Soc.* **2007**, *27*, 4021–4024.

[171] Lu, S. G.; Rozic, B.; Zhang, Q. M.; Kutnjak, Z.; Pirc, R.; Lin, M.; Li, X.; Gorny, L. *Appl. Phys. Lett.* **2010**, *97*, 202901.

[172] Moya, X.; Stern-Taulats, E.; Crossley, S.; González-Alonso, D.; Kar-Narayan, S.; Planes, A.; Mañosa, L.; Mathur, N. D. *Adv. Mater.* **2013**, *25*, 1360–1365.

[173] Bai, Y.; Zheng, G.; Shi, S. *Appl. Phys. Lett.* **2010**, *96*, 192902.

[174] Hlinka, J.; Márton *Phys. Rev. B.* **2006**, *74*, 104104–1–12.

[175] Ong, L.-H.; Osman, J.; Tilley, D. R. *Phys. Rev. B* **2001**, *63*, 144109–1–10.

[176] Merz, W. J. *Phys. Rev.* **1954**, *95*, 690–698.

[177] Shirane, G.; Hoshino, S. *J. Phys. Soc. Jpn.* **1951**, *6*, 265–270.

[178] Rossetti Jr, G. A.; Cross, L. E.; Kushida, K. *Appl. Phys. Lett.* **1991**, *59*, 2524–2526.

[179] Hlinka, J.; Ostapchuk, T.; Nuzhnyy, D.; Petzelt, J.; Kuzel, P.; Kadlec, C.; Vanek, P.; Ponomareva, I.; Bellaiche, L. *Phys. Rev. Lett.* **2008**, *101*, 167402.

[180] Perry, C. H.; Khanna, B. N.; Rupprecht, G. *Phys. Rev.* **1964**, *135*, A408.